

PAPER • OPEN ACCESS

Competing excitation quenching and charge exchange in ultracold Li-Ba⁺ collisions









To cite this article: Xiaodong Xing *et al* 2024 *J. Phys. B: At. Mol. Opt. Phys.* **57** 245201

View the [article online](#) for updates and enhancements.

You may also like

- [Photoelectron momentum distribution in structured strong fields](#)
Abhisek Sinha, Arnab Sen, Sanket Sen et al.
- [Dy³⁺ ions in fluorophosphate glasses for luminescent white light applications](#)
K Venkata Rao, S Vidya Sagar, N V Srihari et al.
- [Quantum effect in a hybrid bose-einstein condensate opto-magnomechanical system](#)
Ziyad Imara, Khadija El Anouz, Farhan Saif et al.

Competing excitation quenching and charge exchange in ultracold Li-Ba⁺ collisions

Xiaodong Xing^{1,2} , Pascal Weckesser^{3,4,5} , Fabian Thielemann³ , Tibor Jónás^{1,6,7,*} , Romain Vexiau¹ , Nadia Bouloufa-Maafa¹ , Eliane Luc-Koenig¹, Kirk W Madison⁸ , Andrea Orbán⁷ , Ting Xie⁹ , Tobias Schaetz^{3,10}  and Olivier Dulieu¹ 

¹ Laboratoire Aimé Cotton, Université Paris-Saclay, CNRS, Orsay 91400, France

² School of Quantum Information Future Technology, Henan University, Zhengzhou 450046, People's Republic of China

³ Albert-Ludwigs-Universität Freiburg, Physikalisches Institut, 79104 Freiburg, Germany

⁴ Max-Planck-Institut für Quantenoptik, 85748 Garching, Germany

⁵ Munich Center for Quantum Science and Technology (MCQST), 80799 Munich, Germany

⁶ University of Debrecen, Doctoral School of Physics, Egyetem tér 1., 4032 Debrecen Hungary

⁷ HUN-REN Institute for Nuclear Research (ATOMKI), Bem tér 18/c, 4026 Debrecen, Hungary

⁸ Department of Physics and Astronomy, University of British Columbia, Vancouver, BC V6T1Z1, Canada

⁹ State Key Laboratory of Molecular Reaction Dynamics, Dalian Institute of Chemical Physics, Chinese Academy of Sciences, Dalian, Liaoning 116023, People's Republic of China

¹⁰ EUCOR Centre for Quantum Science and Quantum Computing, Albert-Ludwigs-Universität Freiburg 79104, Germany

E-mail: jonas.tibor@atomki.hu

Received 22 June 2024, revised 30 September 2024

Accepted for publication 22 October 2024

Published 20 November 2024



CrossMark

Abstract

Hybrid atom-ion systems are a rich and powerful platform for studying chemical reactions, as they feature both excellent control over the electronic state preparation and readout as well as a versatile tunability over the scattering energy, ranging from the few-partial wave regime to the quantum regime. In this work, we make use of these excellent control knobs, and present a joint experimental and theoretical study of the collisions of a single ¹³⁸Ba⁺ ion prepared in the $5d^2D_{3/2,5/2}$ metastable states with a ground state ⁶Li gas near quantum degeneracy. We show that in contrast to previously reported atom-ion mixtures, several non-radiative processes, including charge exchange, excitation exchange and quenching, compete with each other due to the inherent complexity of the ion-atom molecular structure. We present a full quantum model based on high-level electronic structure calculations involving spin-orbit couplings. Results are

* Author to whom any correspondence should be addressed.



Original Content from this work may be used under the terms of the [Creative Commons Attribution 4.0 licence](https://creativecommons.org/licenses/by/4.0/). Any further distribution of this work must maintain attribution to the author(s) and the title of the work, journal citation and DOI.

in excellent agreement with observations, highlighting the strong coupling between the internal angular momenta and the mechanical rotation of the colliding pair, which is relevant in any other hybrid system composed of an alkali-metal atom and an alkaline-earth ion.

Keywords: coupled-channel equations, spin-orbit coupling, hybrid traps, ultracold atom-ion collisions

1. Introduction

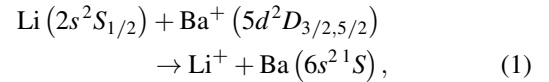
Quantum mixtures of ultracold atomic gases are powerful platforms for opening new perspectives on dilute and condensed matter physics, due to their exquisite level of control that can be achieved in the experiments. Using neutral particles, various arrangements can be studied as for instance mixtures of quantum gases of different species, of identical species but in different quantum states, or immersion of a single impurity inside a quantum gases [1]. Another promising mixed system recently emerges in the form of hybrid traps, i.e. the merger of a single or a few laser-cooled and trapped atomic ions and an ultracold quantum atomic gas [2, 3]. Such platforms offer opportunities to investigate quantum effects in ultracold ion-atom interaction, ultracold chemistry, formation of ultracold molecular ions for precision measurements, dynamics of a charged impurity in a neutral gas. An immediate question is raised: how stable are these hybrid systems? Due to the range of the ion-neutral interaction (varying as R^{-4} , with R the interparticle distance) being much longer than the neutral-neutral interaction (varying as R^{-6}), three-body recombination events involving an ion and two neutrals is likely to occur [4–7], hampering the stability of such hybrid systems. However considering the inherent many-body nature of these mixtures, other perspectives can be envisioned, like the solvation of an ion within the atomic bath [8], or the formation of ion-atom complexes assisted by the trap potential [9, 10].

The ion-neutral physics intrinsically depends on the details of the two-body interactions. Focusing on ion-atom hybrid systems, a wealth of experiments have been developed with various combinations, either homonuclear ones [11–13], or heteronuclear pairs of alkali-metal (AM) atoms an alkaline-earth (AE) ions (or Yb^+) [14–24]. As the laser-cooling scheme involves the metastable state of the AE ion, the hybrid trap offers access to the collisional dynamics of ion-atom systems in the electronically excited states, with high internal energy disposal, opening the possibility for charge exchange (CE) [20, 25, 26]. Numerous recent experiments revealed that excitation exchange between the two particles is the dominant channel [27]. Simplified collisional calculations using high-level electronic structure of the related molecular complex [AM-AE]⁺ have been used to elucidate this diversity for various systems like LiCa^+ [26], RbSr^+ [27], RbBa^+ [6], RbCa^+ [28]. But observed scattering rates are still missing a full quantitative interpretation, emphasizing that more elaborated dynamical models must be employed.

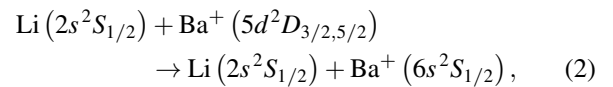
In this work, we focus on an ion-atom combination, a $^{138}\text{Ba}^+$ ion interacting with ^6Li atoms, with a large mass

imbalance suitable for reaching the quantum regime of ultracold collisions [29, 30]. Among all such pairs of AE ions and AM atoms, the entrance ground-state scattering channel $\text{Ba}^+ + \text{Li}$ has the lowest energy, such that the system is protected against radiative CE (the channel $\text{Ba} + \text{Li}^+$ is closed). This feature is particularly suitable for the observation of magnetic Feshbach resonances (MFRs) [31–33], a crucial step toward the quantum control of the collision, the formation of ultracold molecular ions [34] and for ultracold chemistry [2]. Adding internal energy in the particles by electronic excitation enriches the multiplicity of dynamical pathways to be investigated. In particular, the laser cooling scheme of the ion involves the lowest metastable state, namely $5d^2D$ for the Ba^+ ion, allowing for the observation of excited ion collisions with neutral atoms. Such collisions have been observed in various systems, and were initially thought to be dominated by CE [16, 19, 20, 23, 25, 26, 35], but these collisions also exhibit an interplay between other strong scattering channels leading to excitation exchange and quenching [6, 27].

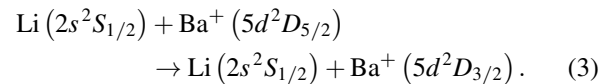
In our system, we observe yet a different dynamical pattern. Several processes are found to compete with each other with comparable rates, as illustrated in figure 1: the *non-radiative charge exchange* (NRCE)



the *non-radiative quenching* (NRQ)



and the *fine-structure quenching* (FSQ)



Note that radiative processes like spontaneous emission and radiative association can be safely neglected, as their rate coefficients are expected to be three orders of magnitude weaker than the above scattering processes (see for instance [28, 36]).

In the rest of the paper we adopt the shortened notations $\text{Li}(2S_{1/2})$, $\text{Ba}^+(5D_{3/2})$, $\text{Ba}^+(5D_{5/2})$, and $\text{Ba}(^1S)$ for the atomic states. Occasionally, the entrance channel in equations (1) and (2) will be referred to as S+D, the outgoing channel in equation (1) as Ion+S, and the outgoing channel in equation (2) as S+S.

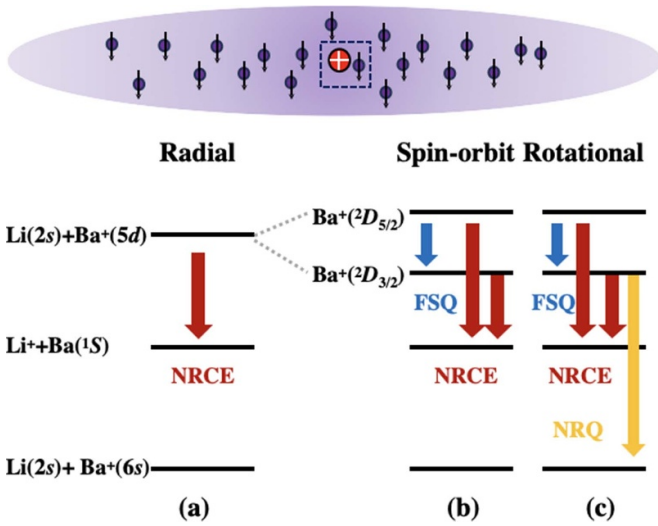


Figure 1. Schematic diagram of the energy levels of the $[\text{Li}, \text{Ba}]^+$ pair relevant for the present work, revealing the possible processes (non-radiative charge exchange (NRCE), non-radiative quenching (NRQ), fine-structure quenching (FSQ)) as the hierarchy of internal couplings are considered: dynamical radial coupling for (a), (b) and (c), the spin-orbit coupling for (b) and (c), and the rotational coupling for (c).

The paper is structured as follows. We first recall in section 2 the main features of the experimental setup and the observed rates for the various processes. In section 3 we present the electronic structure of the LiBa^+ molecular ion, including our computed potential energy curves (PECs) and spin-orbit couplings (SOCs), and characterize their main features in terms of a simple Landau-Zener dynamical model, which is found insufficient to interpret the observations. Thus in section 4 we propose two quantum scattering models including SOC with and without the rotational (Coriolis) coupling, confirming the interplay between them, as it was anticipated in [27]. Additional information regarding experimental setup and theoretical methods are provided in the appendix.

2. Experimental results

In the hybrid setup in Freiburg, we combine a segmented linear Paul trap with an all-in-one-spot ultracold atom apparatus. A detailed description of the setup and various techniques has been presented in previous work [32, 37] and are further elaborated in appendices A–C.

At the beginning of each experimental sequence, we deterministically capture and prepare individual $^{138}\text{Ba}^+$ ions [32, 38], by cooling them close to the Doppler temperature $T_D \sim 365 \mu\text{K}$. We compensate for radial and axial stray electric fields down to $\lesssim 5 \text{ mV m}^{-1}$. For the interaction with the ^6Li atoms we then either prepare the ion in the $5D_{3/2}$ or $5D_{5/2}$ electronic manifold (figures 1 and 2). Their respective radiative lifetime is 80 s and 32 s, which are orders of magnitude longer than the duration of the experimental sequence, so that any change of internal state is induced by collisions.

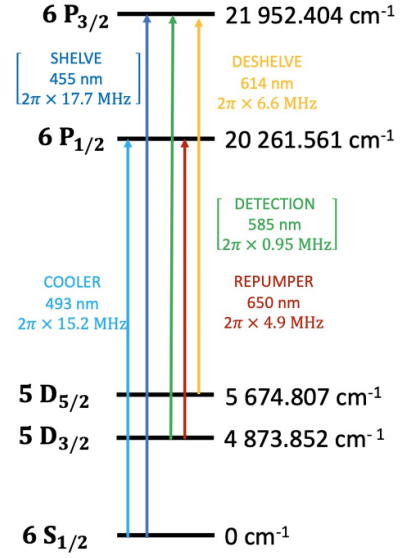


Figure 2. Energy levels of $^{138}\text{Ba}^+$, and relevant laser wavelengths for its cooling and its detection (see appendix A). The brackets refers to lasers which were not available at the time of the present experiment.

Once prepared, we then shuttle the ion along the axial direction to subsequently prepare the Li cloud.

For the ^6Li atoms, we first load a magneto-optical trap (MOT) at the center of the Paul trap. We then transfer the atoms into a crossed optical-dipole trap (xODT) and perform evaporative cooling at higher magnetic fields close to quantum degeneracy, thus reaching a density n . After evaporation we prepare the Li atoms in the level that correlates to the $|f = 1/2, m_f = -1/2\rangle$ sublevel at zero magnetic field, where f is the Li total angular momentum (including electronic and nuclear spin) and m_f its projection onto the quantization axis. Maintaining the magnetic field $B = 293 \text{ G}$ we then transfer the ion back to the trap center where the atoms reside.

After an interaction duration t_{int} , we probe the resulting ion state, distinguishing between direct ion detection, a hot ion, an ion in the $5D_{5/2}$ state or loss of the ion from the trap. Typical experimental measurements are displayed in figure 3 for both $5D_{3/2}$ and $5D_{5/2}$ Ba^+ state preparation. Further details are provided in appendix B. We measured the survival probability of the ion with respect to t_{int} , and with respect to the number of so-called Langevin collisions: it is defined as the expected maximal number of collisions per second $\mathcal{R}_L = 2\pi n \sqrt{2C_4/\mu}$, determined by the classical Langevin capture model, with the reduced mass μ of the colliding pair, and the induced dipole coefficient C_4 . An event is categorized as a survival if the ion remains in the state it was initially prepared: such events are referred to as elastic collisions (EC) counts. The data are fitted with an exponential function. A total of 510 and 116 events were observed for Ba^+ prepared in $5D_{3/2}$ and $5D_{5/2}$ state, respectively. The contributions of the NRCE, NRQ and FSQ processes are presented as fractions of the total number of inelastic counts (thus excluding EC counts). The branching ratio for the various processes are expressed

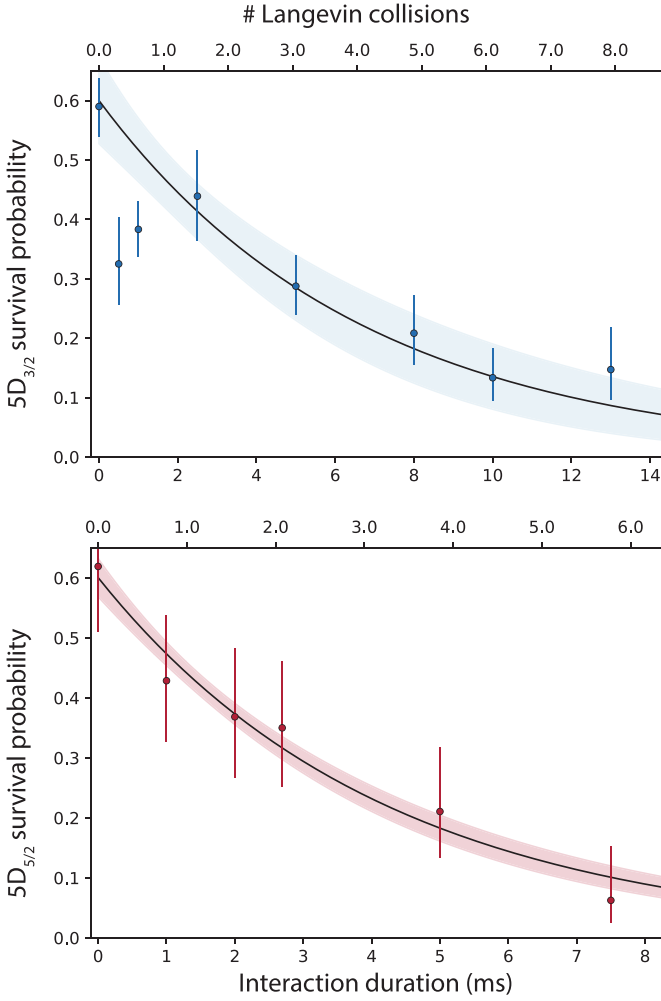


Figure 3. Survival probability P_{sur} of single $\text{Ba}^+(5^2D_{3/2})$ (top panel) or $\text{Ba}^+(5^2D_{5/2})$ (bottom panel) ion as a function of the interaction duration t_{int} with the Li atoms, expressed in ms, and in terms of number of Langevin collisions (appendix B). Each point corresponds to an average over at least 20 events, while the error bars represent the 1σ -confidence interval. The black curves are exponential fits $P_{\text{sur}} = e^{-\Gamma t_{\text{int}}}$, with $\Gamma_{3/2} = 0.17(5)_{\text{stat}}(3)_{\text{sys}}$ and $\Gamma_{5/2} = 0.30(4)_{\text{stat}}(6)_{\text{sys}}$. The statistical error (*stat*) arises from the fit, whereas the systematic error (*sys*) originates from the density uncertainty of the Li cloud. The shaded area indicates the uncertainty of the fits. The non-unity survival probability for small t_{int} values is due to ion losses that occur during its movement through, and interaction with, the finite-size atomic cloud on its way to the center of the trap.

as fractions of the process rate coefficients normalized by the experimental Langevin rate coefficients $K_L^{\text{exp}}(5D_{3/2,5/2}) = \mathcal{R}_L/n$. The results are presented in table 1, together with those of the theoretical models discussed in the next sections.

3. Electronic structure of the LiBa^+ system

Describing inelastic processes requires an accurate model for the PECs of the LiBa^+ molecule, including those of the excited electronic states, and their couplings. In this section, we present our calculations of the electronic PECs in Hund's

case (a) in the molecular frame, and their SOCs. We then propose first a simple semiclassical model for the collision in the molecular frame, thus ignoring the mechanical rotation of the colliding particles.

Hund's case (a) PECs. We first calculate the LiBa^+ PECs without spin-orbit interaction following the methodology of our previous papers (see [39–41] and references therein). Briefly, we represent the Li^+ and Ba^{2+} ionic cores by effective core potentials completed by core polarization potentials to account for electronic valence-core correlation. Thus only two valence electrons are considered, and the wavefunctions are represented using a large Gaussian basis set. All relevant parameters are reported in the references above. The two-electron Hamiltonian is expressed in this basis, and a full configuration interaction is performed to yield PECs in the body-fixed (BF) frame up to the tenth dissociation limit $\text{Li}(2s) + \text{Ba}^+(6p)$. At large internuclear distances R , the PECs dissociating into a ground-state Li atom and the Ba^+ ion are extrapolated by the term $-C_4/R^4 - C_6/R^6$, where $C_4 = 82.2 \text{ a.u.}$ is half the static dipole polarizability of the Li atom, calculated within the present basis representation for the sake of consistency [42]. The C_6 coefficients used in the calculations can be found in appendix D.

The computed Hund's case (a) PECs are displayed in figure 4. The corresponding numerical data are provided in the supplementary material (SM). We immediately see that the three lowest dissociation limits of relevance here are quite well isolated from upper ones, in contrast for instance with heavier similar systems like RbBa^+ [6] and RbSr^+ [27, 40]. Our results are consistent with the recent calculations of LiBa^+ electronic structure [32, 43, 44] with a different approach (see appendix D for more details). The most remarkable feature is the avoided crossing (hereafter referred to as the X_1 crossing) of the $3^1\Sigma^+$ PEC correlated to the $\text{Li}(2s) + \text{Ba}^+(5d)$ entrance channel with the $2^1\Sigma^+$ PEC around 11 a.u. (1 a.u. = 0.05 291 7721 092 nm), which will be the main cause of NRCE. It is worth noting that the occurrence of such a crossing in the PECs in the similar entrance channel in the other systems of the same family is not general: the RbBa^+ PECs display an avoided crossing in the $3^1\Pi$ symmetry [6, 19], the LiCa^+ PECs in the $3^3\Sigma^+$ symmetry [26], the RbSr^+ PECs in the $1^1\Sigma^+$ and $3^3\Sigma^+$ symmetries [27], and the RbCa^+ PECs in the $1^1\Sigma^+$, $3^3\Sigma^+$, $1^1\Pi$ and $3^3\Pi$ symmetries [16, 25, 28]. This illustrates the variety of the dynamics that can be expected with this class of systems in hybrid traps. Another remarkable feature of the LiBa^+ species is the presence of a crossing between the $1^3\Sigma^+$ and the $1^3\Pi$ around 6 a.u. (hereafter referred to as the X_3 crossing) which is responsible for the additional complexity of the MFRs in the ground state manifold [32].

Spin-orbit couplings. The R -dependent SOCs are obtained following the same quasidiabatic approach extensively described in our previous paper on RbCa^+ [28], inspired by earlier works [45, 46]. The corresponding numerical data are provided in the SM. We recall here the main steps for convenience. A set of reference basis vectors $\{|R_1\rangle \dots |R_N\rangle\}$ ($N = 30$ here) is defined as the eigenvectors of the electronic Hamiltonian at large internuclear distance (60 a.u.), thus yielding a representation of the separated atom states. A

Table 1. Experimental and theoretical rate coefficients for repeated sequences of collision events of a single Ba^+ ion prepared in the $5D_{3/2}$ or $5D_{5/2}$ state with ground state Li atoms. The total number of counts is displayed for survival events (or EC for elastic collisions), and for each inelastic (NRQ, FSQ) or reactive (NRCE) process, as well as their ratio abundance (%) with respect to the number of counts excluding EC ones. They are converted into branching ratios, or probability per Langevin collision, after normalizing experimental rate coefficients by Langevin rate coefficients ($K_{\text{exp}}/K_L^{\text{exp}}$). The statistical error (*stat*) arises from the fit, whereas the systematic error (*sys*) originates from the density uncertainty of the Li cloud. The theoretical non-thermalized reaction rate coefficients per Langevin collision $K_{\text{MCQS}}/K_L^{\text{th}}$ are computed for a collisional (center-of-mass) energy E_i expressed as $T_{\text{eff}} = E_i/k_B$ of $30 \mu\text{K}$, consistent with experimental conditions. We estimate a rate $K_{\text{MCQS-L}}$ from a Langevin average of K_{MCQS} (see section 4), thus yielding a range of acceptable theoretical values displayed in the last column.

Event	Process	Counts	Ratio(%)	$K_{\text{exp.}}/K_L^{\text{exp}}$	$K_{\text{MCQS}}/K_L^{\text{th}}; K_{\text{MCQS-L}}/K_L^{\text{th}}$
$5D_{3/2}$: $K_L^{\text{exp}} = 4.69 \times 10^{-9} \text{ cm}^3 \text{ s}^{-1}$; $K_L^{\text{th}} = 4.81 \times 10^{-9} \text{ cm}^3 \text{ s}^{-1}$					
	EC	177	—	—	—
Hot	NRQ	302	90.6(16)	0.154(45) _{stat} (27) _{sys}	0.21;0.18
Loss	NRCE	31	9.4(16)	0.016(5) _{stat} (3) _{sys}	0.021;0.012
Total		510			
$5D_{5/2}$: $K_L^{\text{exp}} = 4.81 \times 10^{-9} \text{ cm}^3 \text{ s}^{-1}$; $K_L^{\text{th}} = 4.81 \times 10^{-9} \text{ cm}^3 \text{ s}^{-1}$					
	EC	41	—	—	—
Cold+Hot	FSQ	42+8	66(6)	0.198(26) _{stat} (40) _{sys}	1.06;0.725
Loss	NRCE	25	34(6)	0.102(14) _{stat} (20) _{sys}	0.052;0.16
Total		116			

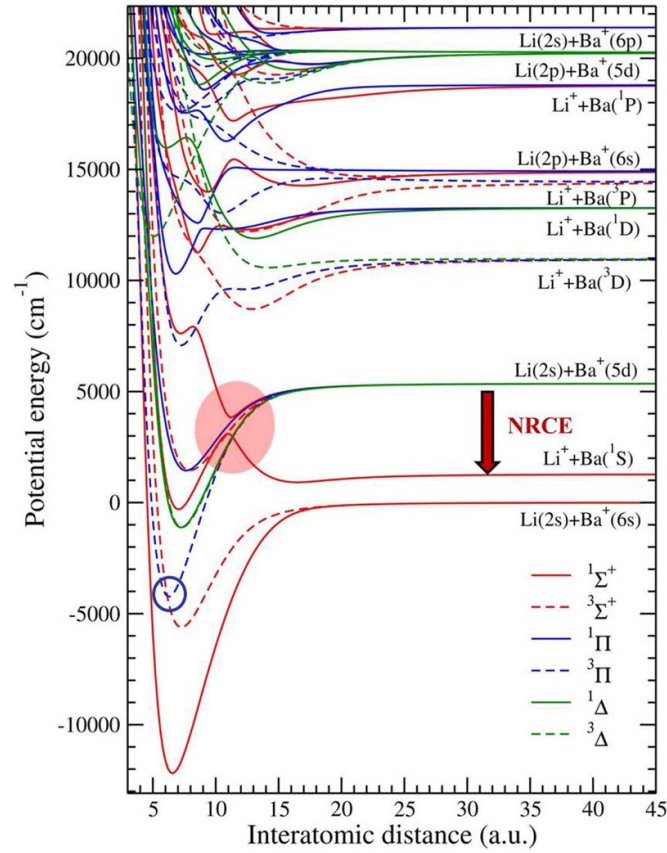


Figure 4. LiBa^+ Hund's case (a) PECs in the BF frame up to the $\text{Li}(2s)+\text{Ba}^+(6p)$ dissociation limit. The red area locates the X_1 avoided crossing between the $2^1\Sigma^+$ and $3^1\Sigma^+$ PECs, inducing NRCE. The blue circle locates the X_3 crossing between the $1^3\Sigma^+$ and $1^3\Pi$ PECs.

unitary transformation is then applied to express the N lowest adiabatic states $[|\Psi_1^0\rangle \dots |\Psi_N^0\rangle]$ at arbitrary R on the reference basis set $[|R_1\rangle \dots |R_N\rangle]$, leading to a quasidiabatic electronic Hamiltonian represented in the separated atom basis. The atomic SOCs are then added to it for the 7 lowest asymptotes, up to $\text{Li}(2p)+\text{Ba}^+(6s)$, opening two options: either a full diagonalization of this Hamiltonian to obtain adiabatic PECs including spin-orbit, or to perform the inverse unitary transformation to retrieve SOCs between Hund's case (a) adiabatic states. The latter is displayed in figure 5 for the three lowest dissociation limits for the Hund's case symmetries labeled with the projection on the molecular axis of the total electronic angular momentum $\Omega = 0^{+/-}, 1, 2, 3$. They are labeled according to the notations of the matrix elements of the potential energy matrix reported in table 2. As expected, the couplings between states correlated to the $\text{Li}(2s)+\text{Ba}^+(5d)$ asymptote converge toward the relevant atomic values (the atomic spin-orbit splitting between $\text{Ba}^+(5^2D_{5/2})$ and $\text{Ba}^+(5^2D_{3/2})$ is 800.955 cm^{-1}), while those couplings for states correlated to different asymptotes vanish at large distances.

Landau-Zener modeling. The X_1 avoided crossing requires attention prior to the scattering calculations, as it induces NRCE. We first check its efficiency using a simple Landau-Zener (LZ) model [47], linearizing the avoided crossing at $R_{X1} = 11.06 \text{ a.u.}$ where the PECs are split by $2W_{X1} = 0.00359 \text{ a.u.}$ (or 781.7 cm^{-1}) (see appendix E). We obtain a single-path probability $P_{LZ} = 0.769$ and a double-path probability $2P_{LZ}(1 - P_{LZ}) = 0.355$, suggesting that the crossing is quite efficient. At this level of the theory, assuming a statistical population of the initial states, the NRCE probability amounts to $P_{LZ}^{\text{NRCE}} = 0.355/20 = 0.0177$, clearly far too small compared to the observations (table 1). In the next section, this linearization of the X_1 crossing will be used to model the interaction around R_{X1} (see table 2) using a Gaussian expression $G = W_{X1} \exp(-(R - R_{X1})^2/2\delta^2)$, with $W_{X1} = 0.001795 \text{ a.u.}$, and a full width $\Gamma = 2\sqrt{2 \ln(2)}\delta$ with $\delta = 0.75 \text{ a.u.}$. We checked the sensitivity of the dynamical calculations of the next section with the empirically chosen width by varying it as $\delta = 0.75 \pm 0.5 \text{ a.u.}$, and did not observed any significant effect. The W_{X1} parameter is well defined by the PECs.

We can introduce FSQ in such a simple model by considering the $\Omega = 0^+$ block in table 2, diagonalizing it, and setting up a multicrossing LZ model (see appendix E). An important issue raises here. The marked X_1 avoided crossing indicates that the two involved $1^1\Sigma^+$ states quite abruptly exchange their electronic character in this region. As we linearized the X_1 crossing around R_{X1} , we must take into account this diabaticization in the SOCs coupling. This is illustrated in figure 5(a): a marked inversion between $A_{2,4}$ and $A_{3,4}$ coupling reflects the presence of the X_1 avoided crossing in the related PECs, so that we diabaticized these couplings by smoothly joining their left and right branches along the black dashed lines. However the computed probabilities are still in disagreement with the experimental data, as it was the case too in the analysis of $\text{Rb}+\text{Sr}^+$ collisions [27].

When modeled in molecular frame (see next section) this avoided crossing generates a complicated multi-crossing pattern of the PECs in the space-fixed frame. Therefore, the LZ

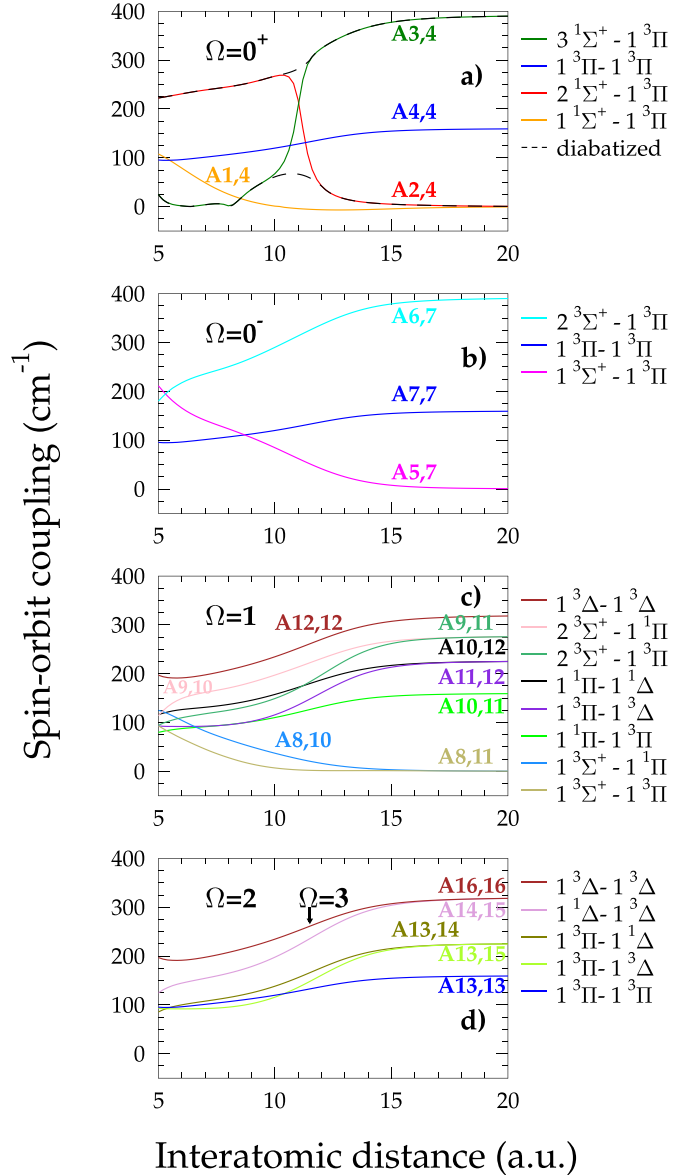


Figure 5. Computed R -dependent SOCs (using notations of table 2) between the states correlated to the three lowest LiBa^+ dissociation limits, for (a) $\Omega = 0^+$, (b) $\Omega = 0^-$, (c) $\Omega = 1$, (d) $\Omega = 2, 3$. In panel (a), the diabaticized coupling resulting from the linearization of the X_1 avoided crossing is drawn as a dashed black line.

model is not adapted anymore to describe the dynamics, as it misses the complex situation of many interfering wavefunctions in the zone of these multiple avoided crossings. This also results in a population of the molecular states very different from the statistical one assumed here. Full quantum scattering calculations must be performed.

4. Quantum scattering models

In this section, we first extend the previous four-channel semiclassical model by solving quantum coupled equations in the molecular frame. The dynamics must be treated in the space-fixed (SF) frame, necessitating first the determination of the PECs in Hund's case (e), including the mechanical rotation

Table 2. Schematic view of the 16×16 potential energy symmetric matrix in the BF frame, involving the Hund's case (a) molecular states correlated to the three lowest LiBa^+ dissociation limits $\text{Li}(2s) + \text{Ba}^+(6s)$, $\text{Li}^+ + \text{Ba}(6s^2 1S)$, $\text{Li}(2s) + \text{Ba}^+(5d)$, denoted S+S, Ion+S, and S+D, respectively. All blank cells corresponds to zero matrix elements. The $G_{2,3} \equiv G_{2,3}$ elements refers to the Gaussian coupling associated to the X_1 avoided crossing. The $A_{8,11} \equiv A_{11,8}$ is the coupling associated with the X_3 crossing.

	$\Omega=0^+$				$\Omega=0^-$			$\Omega=1$				$\Omega=2$			$\Omega=3$	
	S+S	Ion+S	S+D		S+S	S+D		S+S	S+D			S+D			S+D	
	$1^1\Sigma^+$	$2^1\Sigma^+$	$3^1\Sigma^+$	$1^3\Pi$	$1^3\Sigma^+$	$2^3\Sigma^+$	$1^3\Pi$	$1^3\Sigma^+$	$2^3\Sigma^+$	$1^1\Pi$	$1^3\Pi$	$1^3\Delta$	$1^3\Pi$	$1^1\Delta$	$1^3\Delta$	$1^3\Delta$
$1^1\Sigma^+$	$V(1^1\Sigma^+)$	0	0	$A_{1,4}$												
$2^1\Sigma^+$	0	$V(2^1\Sigma^+)$	$G_{2,3}$	$A_{2,4}$												
$3^1\Sigma^+$	0	$G_{3,2}$	$V(3^1\Sigma^+)$	$A_{3,4}$												
$1^3\Pi$	$A_{4,1}$	$A_{4,2}$	$A_{4,3}$	$V(1^3\Pi) + A_{4,4}$												
$1^3\Sigma^+$					$V(1^3\Sigma^+)$	0	$A_{5,7}$									
$2^3\Sigma^+$					0	$V(2^3\Sigma^+)$	$A_{6,7}$									
$1^3\Pi$					$A_{7,5}$	$A_{7,6}$	$V(1^3\Pi) + A_{7,7}$									
$1^3\Sigma^+$								$V(1^3\Sigma^+)$	0	$A_{8,10}$	$A_{8,11}$	0				
$2^3\Sigma^+$								0	$V(2^3\Sigma^+)$	$A_{9,10}$	$A_{9,11}$	0				
$1^1\Pi$								$A_{10,8}$	$A_{10,9}$	$V(1^1\Pi)$	$A_{10,11}$	$A_{10,12}$				
$1^3\Pi$								$A_{11,8}$	$A_{11,9}$	$A_{11,10}$	$V(1^3\Pi)$	$A_{11,12}$				
$1^3\Delta$								0	0	$A_{12,10}$	$A_{12,11}$	$V(1^3\Delta) + A_{12,12}$				
$1^3\Pi$													$V(1^3\Pi) + A_{13,13}$	$A_{13,14}$	$A_{13,15}$	
$1^1\Delta$													$A_{14,13}$	$V(1^1\Delta)$	$A_{14,15}$	
$1^3\Delta$													$A_{15,13}$	$A_{15,14}$	$V(1^3\Delta)$	
$1^3\Delta$																$V(1^3\Delta) + A_{16,16}$

of the colliding particles. We ignore the hyperfine interaction here. First, it is expected that the molecular states with $\Omega = 0^+$ symmetry (which are concerned by the X_1 avoided crossing) have a very small (\approx MHz) hyperfine structure (see for instance [48] for a study on a similar system). Such a coupling is negligible with respect to the electronic and spin-orbit ones. Second, the experiment operates with an external magnetic field of 297 G, and Li atoms are polarized in the $|f = 1/2; m_f = -1/2\rangle$ hyperfine sublevel. The corresponding Zeeman interaction term in the Hamiltonian is negligible too. From the point of view of the unpolarized ion, the orientation of the Li polarization is irrelevant. The chosen value of f may have some consequences on the dynamics, which are not taken into account in our computations.

Four-channel quantum scattering (FCQS) model. We set up the FCQS model by extending the previous semiclassical four-channel model. We solve coupled equations in this $\Omega = 0^+$ subspace in the SF frame, but first neglecting the coupling between the internal angular momenta of the atoms and their relative motional angular momentum with momentum ℓ , referred to as partial wave in the following (appendix F).

The total cross section for an initial collision energy $E_i = \hbar^2 k_i^2 / 2\mu$ in the entrance channel i towards the final state f is extracted from the off-diagonal elements of the \mathbf{S}_ℓ matrix, resulting in a sum over partial waves ℓ ,

$$\sigma(f \leftarrow i, E_i) = \frac{\pi}{k_i^2} \sum_{\ell} (2\ell + 1) |S_{\ell}(f \leftarrow i)|^2, \quad (4)$$

where $\mu = 10481.62$ a.u. is the LiBa^+ reduced mass.

The calculated partial and total cross sections are presented in figure 6 for the case of the Ba^+ ion prepared either in the $5^2D_{5/2}$ or $5^2D_{3/2}$ state. In both cases, the total cross sections for each process exhibit shape resonances in the entrance channel, every two partial waves ℓ in accordance with the quantum defect asymptotic theory developed in [49]. As expected, the Langevin cross section $\sigma_L = 2\pi C_4^{1/2} E_i^{-1/2}$ resulting from the classical capture model [50] appears as an upper limit for the quantum cross sections. For the $5^2D_{5/2}$ preparation, the NRQ cross section is negligible compared to the NRCE and FSQ ones, consistently with the experimental observations (table 1). But the NRCE is found dominant, in contrast with experiment. A similar conclusion is drawn for the $5^2D_{3/2}$ preparation. Evidently, this quantum scattering approach does not overcome the limitation of the semiclassical LZ models to yield precise cross sections.

Despite the apparent simplicity of the LiBa^+ structure with a single avoided crossing (X_1) the coupling of the internal angular momenta with the rotational angular momentum ℓ must be taken into account, as already anticipated in our treatment of Rb-Sr^+ collisions [27] (which was involving a more complex structure with two avoided crossings).

Multichannel quantum scattering (MCQS) model. We consider the 16×16 potential energy matrix of table 2. We first define the total angular momentum $\vec{J} = \vec{j}_{\text{Li}} + \vec{j}_{\text{Ba}} + \vec{\ell} \equiv \vec{j} + \vec{\ell}$ (with the associated quantum numbers J, j, ℓ), its projection M over a quantization axis in the SF frame, and the total parity p . As we do not consider any external field, the M quantum number will be omitted in the following. The related frame transformation between the Hund's case (a) molecular basis and the

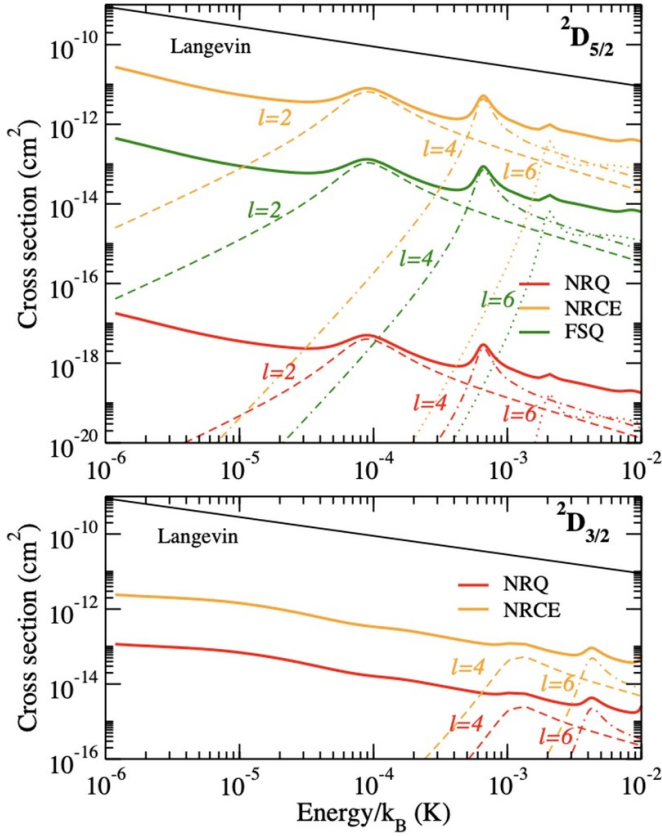


Figure 6. Non-thermalized total cross sections (full lines) computed with the FCQS model as a function of a fixed initial energy expressed as a temperature E_i/k_B , when Ba^+ is prepared either in the $5^2D_{5/2}$ and $5^2D_{3/2}$ state. The partial cross sections for the partial waves inducing shape resonances are drawn with dashed lines. The classical Langevin cross section is displayed as a straight line in this double logarithmic scale.

Hund's case (e) basis expressed in the SF frame is described in appendix G. The relevant quantum numbers for S+S, Ion+S and S+D dissociation limits are reported in appendix G.

Hund's case (e) PECs. They are obtained after diagonalizing the potential energy matrix including rotation for a given J and parity p . The results are reported in figure 7 for $J = 0 - 3$ as representative examples. Indeed, due to available angular momenta (see appendix G), a stable number of channels (12 or 13, depending on the chosen (J, p) combination), is reached for $J \geq 3$. For instance, the $(J = 0, p = +)$ pair only involves the $\Omega = 0^+$ subspace and $\ell = 2$ (figure 7(a)). This difference in the maximal number of channels comes from the contribution of the unique $\Omega = 0^+$ correlated to the *Ion + S* channel, which is present in the (even $J, p = +$) and (odd $J, p = -$) cases, and not for the (odd $J, p = +$) and (even $J, p = -$) cases. At short distances, the Hund's case (e) PECs are very similar to Hund's case (c) PECs, but display more complex structure due to the presence of the rotational (Coriolis) coupling. The X_1 crossing is still prominent, while exhibiting more complex patterns depending on J . One important feature is now that the X_3 crossing at 6.2 a.u. now features an avoided crossing (figures 7(j) and (k)), due to the combined effect of the rotational coupling,

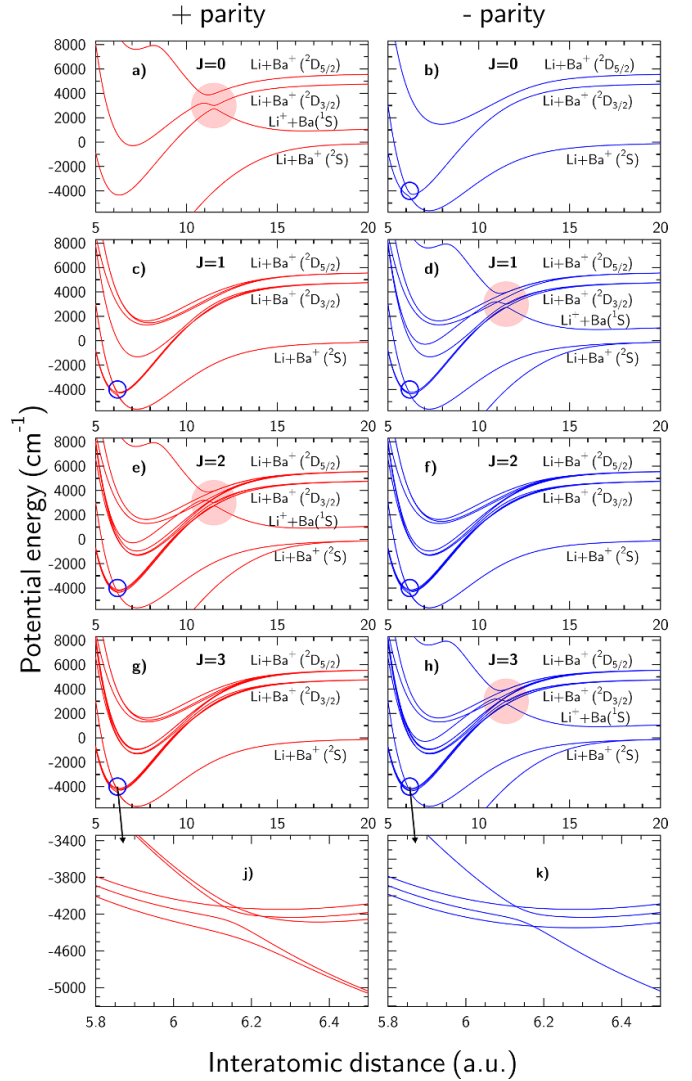


Figure 7. Hund's case (e) potential energy curves for the three dissociation limits S+S, Ion+S, S+D, for + and - parity states. For $J = 0, 1, 2, 3$ and + (resp. -) parity, the number of channels is 4, 8, 12, 12 (resp. 3, 9, 11, 13). The maximal number of channels is reached for $J \geq 3$: it is 12 (resp. 13) for (odd $J, +$) and (even $J, -$) (resp. (even $J, +$) and (odd $J, -$)). Panels (j) and (k) are zoomed PECs around the avoided crossing X_3 marked by blue circles on panels (g) and (h), responsible for NRQ.

and the indirect SOC (the term $A_{8,11}$ in table 2). Therefore we show strong evidence that NRQ is likely to occur in the present experiment. This crossing has been considered in [32] for the modeling of observed MFRs in LiBa^+ . Note that a similar indirect SOC has been invoked in Rb-Yb^+ cold collisions to explain anomalous hyperfine relaxation [51].

Cross sections and rate coefficients. After solving the coupled equations in this basis (appendix F) a \mathbf{S} matrix is obtained for every J value and a given parity p , considering the initial state i with collision energy E_i and an outgoing channel f . It yields the inelastic cross section for a given J and p

$$\sigma(E_i, J, p; f) = \frac{\pi}{k_i^2} \sum_{l_i, j_i} \sum_{l_f, j_f} |S(Jl_i j_i p \leftarrow Jl_f j_f)|^2, \quad (5)$$

while for the elastic cross section

$$\sigma(E_i, J, p; i) = \frac{\pi}{k_i^2} \sum_{l_i, j_i} \sum_{l_f, j_f} |1 - S(Jl_i j_i p \leftarrow Jl_f j_f p)|^2, \quad (6)$$

and then parity-dependent elastic/inelastic cross section

$$\sigma(E_i, p; i/f) = \sum_J (2J+1) \sigma(E_i, J, p; i/f), \quad (7)$$

and finally total cross section

$$\sigma(E_i; i/f) = (\sigma(E_i, +1; i/f) + \sigma(E_i, -1; i/f)) / 2. \quad (8)$$

The $|J, l_i, j_i, p\rangle$ and $|J, l_f, j_f, p\rangle$ vectors represent the chosen initial incoming channels and the allowed final outgoing channels labeled with their quantum numbers valid at infinite distances. The non-thermalized reaction rate is expressed as $K(E_i; f) = (2E_i/\mu)^{1/2} \sigma(E_i; f)$. We define a thermalized reaction rate at the temperature T_{eff} assuming a Maxwell-Boltzmann distribution of relative velocities

$$K(T_{\text{eff}}; f) = \frac{2}{\sqrt{\pi} (k_B T_{\text{eff}})^{3/2}} \times \int_0^\infty K(E; f) \sqrt{E} e^{-E/k_B T_{\text{eff}}} dE. \quad (9)$$

The effective temperature in the center-of-mass [23] $T_{\text{eff}} = (m_{\text{Li}} T_{\text{Ba}^+} + m_{\text{Ba}^+} T_{\text{Li}}) / (m_{\text{Li}} + m_{\text{Ba}^+})$ is determined by the individual temperatures $T_{\text{Ba}^+} \approx 600 \mu\text{K}$ and $T_{\text{Li}} \approx 3 \mu\text{K}$ [32], yielding $T_{\text{eff}} \approx 30 \mu\text{K}$.

It is worth examining the computed cross sections depending on the parity for FSQ, NRCE and NRQ processes, reported in figure 8. The classical Langevin cross section σ_L is reported, as well as partial Langevin cross sections (i.e. for each process) estimated by scaling down σ_L to adjust it to the computed cross sections for energies above $k_B \times 10 \text{ mK}$ where they are expected to be classical, thus behaving as $E_i^{-1/2}$. The cross sections locally exceeds the Langevin rate due to quantum shape resonances associated to specific J values, or partial waves (See appendix H for more insight). The energy location of these resonances is strongly dependent on the molecular data used in the model: they cannot be predicted, and they have to be detected in the experiment. However the model suggests that such resonances contribute to the dynamics at ultralow energies.

Both parity cases exhibit the same dominant process, namely FSQ and NRQ for Ba^+ prepared in the $5D_{5/2}$ and $5D_{3/2}$ state, respectively, which is consistent with the observations. This reveals the strong difference in the structure of the corresponding incoming channels induced by the complex interplay of the various couplings. The NRQ process is found negligible in the $5^2D_{5/2}$ case, in stark contrast with the $5D_{3/2}$ case. This confirms the key importance of the X_3 crossing involving PECs correlated to the $\text{Li}(2S_{1/2}) + \text{Ba}^+(5D_{3/2})$ and the $\text{Li}(2S_{1/2}) + \text{Ba}^+(6S_{1/2})$, see figures 7(j) and (k).

The computed total cross sections $\sigma(E_i; i/f)$ (equation (8)) are presented in figures 9(a) and (b) for the $5D_{5/2}$ and $5D_{3/2}$ cases. The inelastic total cross sections obviously display

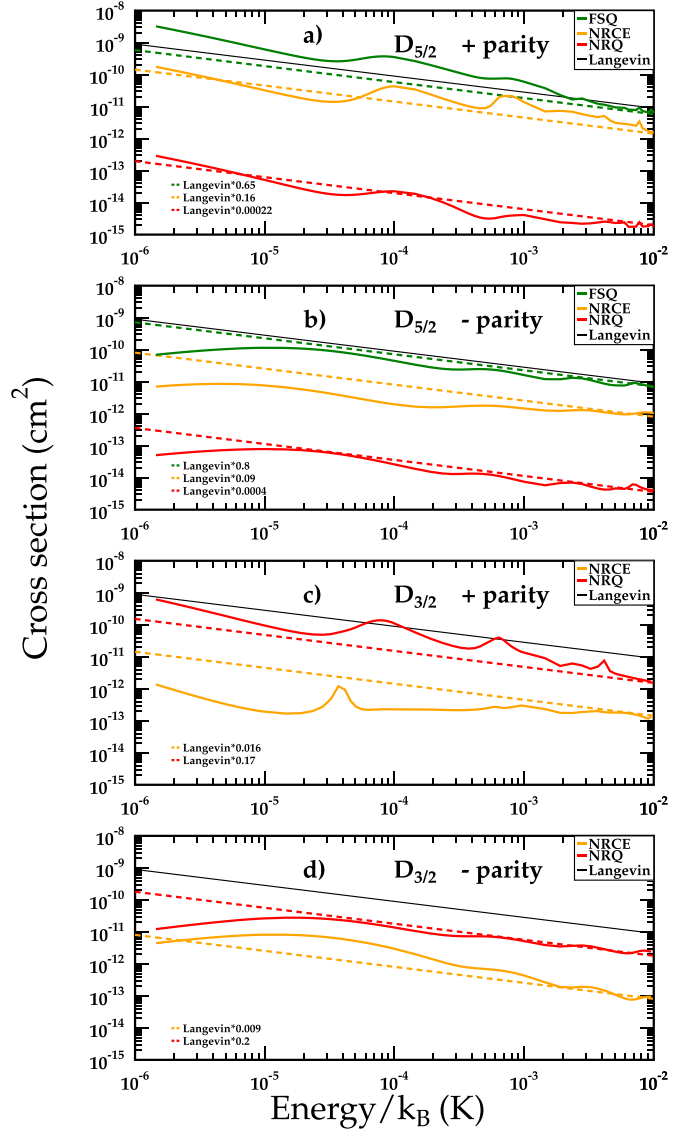


Figure 8. The parity dependent cross sections (equation (7)) as functions of the collision energy (expressed in K), for each allowed process starting from $\text{Li}(2S_{1/2}) + \text{Ba}^+(5D_{5/2})$ (panels (a) and (b)) and from $\text{Li}(2S_{1/2}) + \text{Ba}^+(5D_{3/2})$ (panels (c) and (d)). The Langevin cross section σ_L is displayed (solid black line), as well as scaled Langevin cross sections (dashed colored lines) for each process. The relative contributions of the various processes could be assessed with these scaling factors regardless the presence of scattering resonances. For the $5D_{5/2}$ case, we find $\sigma_L(\text{FSQ}) \approx 4\sigma_L(\text{NRCE}) \approx 3000\sigma_L(\text{NRQ})$ for + parity, and $\sigma_L(\text{FSQ}) \approx 8\sigma_L(\text{NRCE}) \approx 2000\sigma_L(\text{NRQ})$ for - parity. Panel (c) and (d) are for the incoming channels. For the $5D_{3/2}$ case, we find $\sigma_L(\text{NRQ}) \approx 10\sigma_L(\text{NRCE})$ for + parity, and $\sigma_L(\text{NRQ}) \approx 22\sigma_L(\text{NRCE})$ for - parity.

a similar hierarchy between the processes than the parity dependent ones, while the shape resonances are still apparent. They are converted into rates $K(E_i; f)$, and thermally averaged rates $K(T_{\text{eff}}; f)$ (equation (9)) showing that all resonances are smoothed out (figures 9(c) and (d)). The corresponding numerical values are reported in table 1 for the experimental $T_{\text{eff}} = 30 \mu\text{K}$ [32], normalized to the theoretical Langevin rate

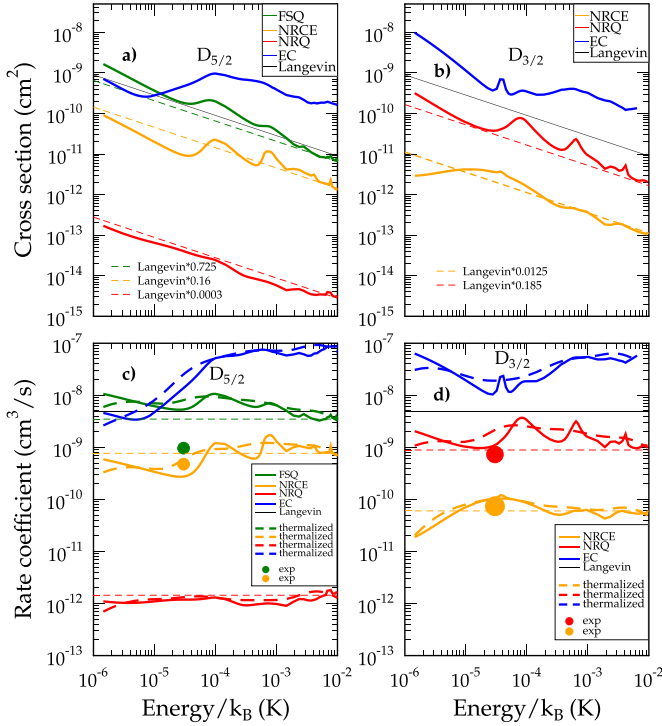


Figure 9. Computed total elastic and inelastic (for each process) cross sections for the $\text{Li}(2S_{1/2})+\text{Ba}^+(5D_{5/2})$ (panel (a)) and $\text{Li}(2S_{1/2})+\text{Ba}^+(5D_{3/2})$ (panel (b)) entrance channels. The Langevin cross section σ_L is displayed (black line), as well as scaled Langevin cross sections (dashed colored lines) for each process. Panels (c) and (d) show the corresponding rate coefficients (colored full lines), the thermalized rate coefficients (thick colored long-dashed lines), the scaled Langevin rate coefficients (dashed colored lines) with the same scaling factors than those for the cross sections, and the Langevin rate coefficient (black line). The full circles are the experimental data of table 1 for $T_{\text{eff}} = 30 \mu\text{K}$, with a circle size consistent with the statistical and systematic errors.

$K_L^{\text{th}} = \sigma_L \times (2k_B T_{\text{eff}}/\mu)^{1/2}$ for appropriate comparison with experimental values.

The theoretical rates are found in remarkable agreement with the measured ones around $T_{\text{eff}} = 30 \mu\text{K}$, which confirms the strong coupling of the internal angular momenta of the particles with their mutual mechanical rotation all along the collision, as it was anticipated in [27]. However, we note the larger discrepancy for the FSQ process in the $\text{Li}(2S_{1/2})+\text{Ba}^+(5D_{5/2})$ entrance channel, for which the computed rate exceeds the measured one by a factor of about 4. It may be due to the inaccuracy of a given SOC resulting from our quasidiabatic method.

The elastic cross sections and rate coefficients deserve a further comment: our calculations predict that ECs dominate the dynamics, with a rate coefficient much larger than the Langevin rate coefficient. This implies that the EC counts reported in table 1 only correspond to the fraction of ECs reflecting the fact that the full capture assumed in the Langevin model is not fulfilled.

5. Discussions and conclusions

In this work, we detected the outcome of the ultracold collisions between a single Ba^+ ion excited in a metastable state immersed in a Li quantum gas close to quantum degeneracy in a hybrid trap. We probed that the dynamics is not restricted to CE, and that several inelastic processes compete with each other and with CE. We measured the branching ratio of these processes, which are found dependent of the initial preparation of the ion. This reveals the complexity of the underlying dynamics. Using a full quantum scattering approach based on high-level electronic structure calculations, we deciphered the main paths, and computed their relative contribution which are found in remarkable agreement with experimental findings, assessing the quality of the molecular data. Similar investigations could be achieved for the same class of systems and will be the topic of future works. It is worth noting the special case of LiYb^+ , in principle very similar to LiBa^+ from the experimental point of view, but which is rather tedious to fully describe theoretically: the open f -shell of the excited Yb and Yb^+ states necessitate the simultaneous consideration of 16 valence electrons, which is far more complicated than in LiBa^+ .

As stated in the paper, the polarization of the Li atoms in the $|f = 1/2, m_f = -1/2\rangle$ state in the reported experiment has not been taken into account in our calculations. In principle, preparing Li atoms in the $f = 3/2$ manifold may influence the dynamics as the molecular states would not be populated in the same way through the frame transformation. This would be even more relevant if both particles were polarized. This will be the purpose of future investigations. This can be accounted for by enlarging the Hilbert space of table 4 in appendix G considering the various projections of the angular momenta in the SF frame as additional good quantum numbers. However we recall that the experimental results on Rb atoms colliding with metastable $\text{Sr}^+(4D_{3/2,5/2})$ ions [27] yielded no evidence of such dependence with respect to the mutual orientation of the spins of the two particles. The latter arises due to Coriolis coupling facilitated by the presence of higher-partial waves.

However, reaching the s -wave regime, while still challenging, would open new experimental possibilities which could help testing theoretical data even more precisely, while allowing additional level of control of the excited state dynamics. In particular, only the $+$ parity manifold would contribute to the excited state dynamics. Moreover, if both particles would be polarized in the largest electronic spin state $m_{\text{Li}} = +1/2$ and $m_{\text{Ba}} = +5/2$, thus only the $^3\Delta(\Omega = 3)$ molecular state would contribute, so that the ion-atom pair would be protected against any non-radiative decay process in the s -wave regime. Such a $^3\Delta$ metastable state has been identified in other species as great candidate for metrology with great sensitivity to magnetic field [52].

In a broader perspective, the PECs of figure 4 illustrates that the light mass of the system results in dissociation thresholds which quite well separated with broad energy gaps, in contrast

with other systems of the same family like RbSr^+ . Thus LiBa^+ Feshbach molecules which would be created from MFR [32, 33] could be protected against photodissociation by the lasers of the setup in the 6000 cm^{-1} – 10000 cm^{-1} approximate range (or roughly 1 – $1.7\text{ }\mu\text{m}$), allowing for longer time to manipulate them. For instance, the X_3 crossing results in a perturbation of the radial wavefunction (see for instance [53]) of the Feshbach molecules due to the indirect SOC matrix element $A_{8,11}$ (table 2). The X_3 crossing happens to be quite aligned with the bottom of the well of the $1^1\Sigma^+$ electronic ground state and of the $2^1\Pi$ state (figure 4). This could represent a pathway for future two-photon experiment aiming at transferring the Feshbach molecules into the lowest vibrational level of ground state LiBa^+ ions.

Data availability statement

All data that support the findings of this study are included within the article (and any supplementary files).

Acknowledgments

This project has received funding from the European Research Council (ERC) under the European Union's Horizon 2020 research and innovation programme (Grant Number 648330), the Deutsche Forschungsgemeinschaft (DFG, Grant Number SCHA 973/9-1-3017959) and the Georg H Endress Foundation. P W gratefully acknowledges financial support from the Studienstiftung des deutschen Volkes. F T and T S acknowledge financial support from the DFG via the RTG DYNCAM 2717. The Hungarian and French teams acknowledge support from the CRNS International Emerging Action (IEA)—ELKH, 2023–2024; Program Hubert Curien 'BALATON' (CampusFranceGrantNo.49848TC); NKFIH TÉT-FR, 2023–2024 (2021-1.2.4- TÉT-2022-00069). A O is grateful for the support of NKFIH FK 132989 Grant. T X acknowledges the support from National Science Foundation of China under Grant No. 22103085.

Appendix A. Experimental protocol

We start each measurement by deterministically preparing a single $^{138}\text{Ba}^+$ ion in our Paul trap. Here we apply a combination of laser ablation loading with two-photon ionization, resulting in a finite number of Doppler cooled ions. Transferring the ion Coulomb crystal into a far-detuned optical dipole trap at 532 nm while switching off the confining radio-frequency fields of the Paul trap, we can deterministically shape the Coulomb crystal down to a single ion [37]. We then use the single ion to compensate our axial and radial stray electric fields down to $\lesssim 3\text{ mV m}^{-1}$ by lowering the confinement of the ion and nulling any observed displacement [54].

For the interaction with the atoms we prepare the ion in either the $5D_{3/2}$ or $5D_{5/2}$ manifold (figure 2). We prepare the $5D_{3/2}$ state by first switching off the $5D_{3/2}$ repumper for 50 ms

while continuing to cool on the D_1 -line (noted COOLER in figure 2). For the $5D_{5/2}$ state, we make use of the off-resonant scattering of our visible (VIS) optical dipole trap [37]. Here, while Doppler cooling, the $^{138}\text{Ba}^+$ ion is illuminated with $\approx 5\text{ W}$ of 532 nm laser light until it is successfully shelved. Once prepared, we then shuttle the ion axially and radially out of the trap center to allow for the preparation of the atomic cloud. Note that both electronic preparation schemes do currently not allow to deterministically prepare a dedicated m_f sublevel.

The ^6Li atoms are loaded in a conventional MOT located at the center of the Paul trap and, after a short compression phase, transferred to the far-detuned crossed optical dipole trap (xODT) operated at 1064 nm . We then evaporatively cool the cloud at $B \approx 345\text{ G}$ to temperatures of $1\text{ }\mu\text{K}$ to $3\text{ }\mu\text{K}$. After evaporation, a $15\text{ }\mu\text{s}$ laser pulse resonant with the $|m_S = -1/2, m_I = 1\rangle \rightarrow P_{3/2}$ transition polarizes the atomic cloud in the $|m_S = -1/2, m_I = 0\rangle$ state, where m_S and m_I are the projection on the magnetic field axis of the electronic and nuclear spin, respectively. Note that for lower magnetic fields the $|m_S = -1/2, m_I = 0\rangle$ state can be expressed as $|f = 1/2, m_f = -1/2\rangle$. We then shift the magnetic field to $B = 293\text{ G}$ where it remains during the interaction phase and the subsequent detection of the atomic cloud. In principle, we can individually align the two xODT beams to the position of the ion with two piezo-controlled mirrors. Overlap between the atomic cloud and the ion is independently verified by measuring the inelastic ion-loss probability for different ion displacements and continuously checked throughout the measurement.

For the interaction we shuttle the ion back to the trap center and let the ion interact with the atomic ensemble for variable time. Afterwards we apply the protocol depicted in figure 10 to detect both the atomic ensemble as well as the outgoing $^{138}\text{Ba}^+$ electronic state. First, we switch off the xODT and after a short time of flight, the atomic cloud is absorption imaged on a closed cycle transition for $15\text{ }\mu\text{s}$ at $B = 293\text{ G}$. The magnetic fields are then ramped down to $B \approx 4\text{ G}$ for $^{138}\text{Ba}^+$ state detection, which consists of three phases.

In each phase the ion is illuminated by different detection lasers for 1 s, followed by a 300 ms fluorescence image (CCD camera). In the first phase, only the Doppler cooling and $5D_{3/2}$ -repumper lasers are switched on. This will reveal ions that are either in the $5D_{3/2}$ - or $6S_{1/2}$ -state with a temperature below $\approx 50\text{ K}$. The latter is limited by the spatial overlap of the cooling beam with the ion. Next we additionally shine in a far-detuned ($\delta \approx 15\Gamma_{\text{nat}}$) Doppler cooling laser with larger waist to recool hot ions with a kinetic energy equivalent to several hundred Kelvin. Finally we apply the $5D_{5/2}$ -repumper to deshelve ions that are in the $5D_{5/2}$ -state after the interaction. If the ion is not detected during any of the phases, the event is classified as a loss, which we attribute to NRCE.

Because we cannot distinguish between the $6S_{1/2}$ - and $5D_{3/2}$ -state, due to the necessity of the $5D_{3/2}$ -repumper for fluorescence detection, we have to interpret the outcome of the first detection phase depending on the initial state of the ion. If the ion is initially prepared in the $5D_{5/2}$ -state, we assume that it has undergone FSQ to the $5D_{3/2}$ -state, because quenching to the $6S_{1/2}$ -state would heat the ion by $\approx 280\text{ K}$,

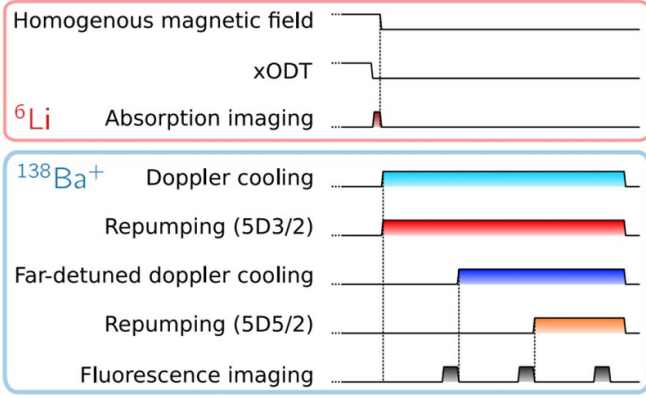


Figure 10. Experimental protocol of the ${}^6\text{Li}$ detection and the subsequent ${}^{138}\text{Ba}^+$ product state detection sequence (durations are not to scale). At the end of the atom-ion interaction phase, the xODT is switched off. After a short expansion duration of $100\ \mu\text{s}$ we perform high-field absorption imaging of the atomic cloud. We then release the magnetic field to 4 G, and detect and classify the ion's electronic state into four possible outcomes. First, the near-detuned Doppler cooling lasers are switched on for 1 s, followed by 300 ms of fluorescence imaging. An ion detected in this stage is classified as *cold* $6S_{1/2}$ or $5D_{3/2}$. Secondly, we switch on a far-detuned cooling beam, also followed by fluorescence detection. An ion appearing in this stage is classified as *hot*. Lastly, we shine in the 614.9 nm repumper to detect whether the ion is shelved in the $5D_{5/2}$ -state. If the ion is not detected after any of the steps, the event is classified as a *loss*.

which is too hot for direct fluorescence detection and recooling. Similarly for an ion initially in the $5D_{3/2}$ -state we assume that it has remained in that state. To obtain the survival probability of an ion in the $5D_{3/2}$ -($5D_{5/2}$)-state, we calculate the relative numbers of ions detected in the first (third) detection phase.

Appendix B. Calibrating the Langevin scattering rate

To compare the observed reaction rates to the Langevin rate K_L , we measure the number of atoms N , the radial trap frequency ω_{rad} , the axial size σ_{ax} and the temperature T of the atomic cloud to obtain the number density $n = \frac{1}{(2\pi)^{3/2}} \frac{m_{\text{Li}} \omega_{\text{rad}}^2}{k_B T \sigma_{\text{ax}}} N$. We adjust the densities for interaction with the ion in the $5D_{3/2}$ or $5D_{5/2}$ state to $n = 1.3(2) \times 10^{11}\ \text{cm}^{-3}$ and $1.6(4) \times 10^{11}\ \text{cm}^{-3}$ respectively. The Langevin collision rate for atom-ion interactions is $\mathcal{R}_L = 2\pi n \sqrt{2} C_4 / \mu$, with the reduced mass μ and the induced dipole coefficient C_4 , which gives $\mathcal{R}_L = 610(100)\ \text{s}^{-1}$ for the $5D_{3/2}$ and $770(180)\ \text{s}^{-1}$ for $5D_{5/2}$ incoming channels. We deduce the Langevin rate coefficients $K_L^{\text{exp}} = 4.81 \times 10^{-9}\ \text{cm}^3\ \text{s}^{-1}$ for $5D_{5/2}$, and $K_L^{\text{exp}} = 4.69 \times 10^{-9}\ \text{cm}^3\ \text{s}^{-1}$ for $5D_{3/2}$ incoming channels. The fit of

the experimental data in figure 3 yields the survival probability $P_{\text{sur}} = 0.30(4)_{\text{stat}}(6)_{\text{sys}}$ of the ion in the $5D_{5/2}$ state, and $P_{\text{sur}} = 0.17(5)_{\text{stat}}(3)_{\text{sys}}$ in the $5D_{3/2}$ state.

In the former case, the observed FSQ process represents 66% of the total events, while the remaining 34% is related to the NRCE process for the $5^2D_{5/2}$ incoming channel (table 1). The rate coefficient for the FSQ process is determined as $0.3 \times 0.66 \times 4.81 \times 10^{-9}\ \text{cm}^3\ \text{s}^{-1} = 0.952 \times 10^{-9}\ \text{cm}^3\ \text{s}^{-1}$, while for the NRCE process as $0.30 \times 0.34 \times 4.81 \times 10^{-9}\ \text{cm}^3\ \text{s}^{-1} = 4.90 \times 10^{-10}\ \text{cm}^3\ \text{s}^{-1}$ (figure 9).

Similarly, in the latter case, the observed NRQ process represents 90.6% of the total events, while the remaining 9.4% is related to the NRCE process (table 1). The rate coefficient for the NRQ process is $0.17 \times 0.906 \times 4.69 \times 10^{-9}\ \text{cm}^3\ \text{s}^{-1} = 7.22 \times 10^{-10}\ \text{cm}^3\ \text{s}^{-1}$, while for the NRCE process is $0.17 \times 0.094 \times 4.69 \times 10^{-9}\ \text{cm}^3\ \text{s}^{-1} = 7.49 \times 10^{-11}\ \text{cm}^3\ \text{s}^{-1}$, see figure 9.

Appendix C. Correcting imperfect $5D_{5/2}$ state preparation

When we conduct experiments with the ion initially in the $5D_{5/2}$ -state, but without the presence of atoms, we observe a cold ion in the first detection phase in 17.5(14)% of all cases. We later identified this to a leakage of 615 nm repumper light into the chamber. As the interaction duration is orders of magnitude shorter than the preparation of the atomic cloud, we can assume that the ion is pumped to the ground state before the interaction begins. Having observed that the $6S_{1/2}$ state is reactionally stable up to 1 s of interaction time at the given densities, we rescale the respective product rate of $5D_{5/2}$ experiments accordingly.

Appendix D. Potentials and spin-orbit couplings

In table 3 we present a comparison of the equilibrium distance and the well depth of our computed PECs with those recently reported in our paper [32] and elsewhere [43, 44] obtained with other computational approaches. While being all consistent with each other, significant dispersion of the results is visible. It is tedious to decide which calculations provide the most accurate predictions, as their accuracy strongly depends on the details of the implementation of each calculation within a given methodology. We recall that our calculations uses a full configuration interaction, in contrast with the other references, which is often an argument in favor of a better accuracy. In contrast, the position of the X_1 and X_3 crossings are very similar in all methods, as well as the energy separation for X_1 . This is encouraging as these are the relevant parameters which control the dynamics treated in the present paper.

Table 3. Equilibrium distance R_e and well depth D_e of the LiBa^+ PECs. The location and energy of the X_1 and X_3 crossings are also given. The van der Waals coefficient C_6 used to extrapolate the PECs at large distance is displayed in the last column.

State	R_e (a.u.)	D_e (cm^{-1})	C_6 (a.u.)
$1^1\Sigma^+$	6.60	12 189	-14820.26
	6.70 [43]	11 627 [43]	
	6.61 [44]	11 846 [44]	
	6.75 [32]	11 860 [32]	
	6.71 [55]	11 674 [55]	
$1^3\Sigma^+$	7.28	5619	-14821.26
	7.56 [43]	4784 [43]	
	7.41 [44]	5401 [44]	
	7.46 [32]	5178 [32]	
$2^1\Sigma^+$	7.02	1580	-21744.76
	7.57 [43]	1206 [43]	
	7.05 [44]	2246 [44]	
$3^1\Sigma^+$	11.20	1524	-2327.73
	10.90 [43]	1833 [43]	
	11.41 [44]	1569 [44]	
$2^3\Sigma^+$	7.98	3905	-2327.73
	7.48 [43]	5961 [43]	
	8.11 [44]	3952 [44]	
$1^1\Pi$	7.60	3915	-3180.61
	7.75 [44]	4034 [44]	
$1^3\Pi$	6.28	9589	-3180.72
	6.42 [43]	8935 [43]	
	6.29 [44]	9390 [44]	
$1^1\Delta$	7.29	6473	-5686.68
	7.18 [43]	5729 [43]	
$1^3\Delta$	7.35 [44]	6250 [44]	
	7.20	6477	-5686.68
X_1	7.42 [44]	6235 [44]	
	11.06	3450	
	10.88 [43]	4171 [43]	
X_3	11.30 [44]	3465 [44]	
	6.15	-4205	
	6.02 [43]	-2326 [43]	
	6.14 [44]	-3973 [44]	

For completeness we also list the C_6 van der Waals coefficient which has been used in addition to the C_4 (identical for all PECs but the $2^1\Sigma^+$) coefficient to fit and extrapolate the PECs at large distances.

Appendix E. Landau Zener model

The Landau–Zener transition probability [47] between two locally linear PECs crossing in R_c for a single path through a crossing is $P_{LZ} = \exp(-2\pi W_c^2/(v_c \Delta F_c))$. The coupling parameter W_c is the energy half-spacing of the two adiabatic PECs in R_c , and ΔF_c is the difference of slopes of the two linearized branches. The relative local velocity of collisions $v_c = \sqrt{2(E_i - U_c)}/\mu$ results from the difference between the initial collision energy E_i and the potential energy U_c in R_c , with μ the reduced mass of the system. In the ultracold regime, E_i is negligible compared to U_c . The double-path probability is obtained according to $2P_{LZ}(1 - P_{LZ})$.

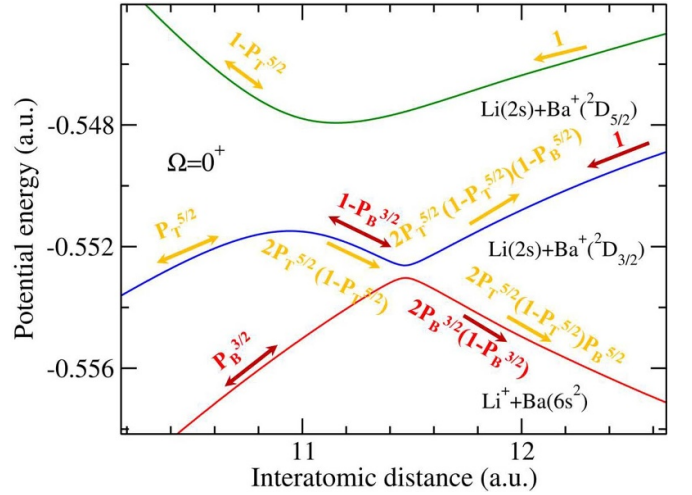


Figure 11. The LiBa^+ PECs around the crossing X_1 after the diagonalization of the $\Omega = 0^+$ submatrix in table 2. The incoming and outgoing LZ probabilities are marked by red and yellow arrows. A unit probability is assumed in the $\text{Li}(2S_{1/2})+\text{Ba}^+(5D_{5/2})$ (yellow arrows) and the $\text{Li}(2S_{1/2})+\text{Ba}^+(5D_{3/2})$ (red arrows) entrance channels.

For the four-channel LZ (FCLZ) model invoked in the main text, figure 11 displays the shape of the corresponding PECs around R_{X1} after diagonalizing the $\Omega = 0^+$ submatrix in table 2, with the corresponding partial probabilities. Labeling with T and B the upper and the lower avoided crossings in the figure, the single-path probabilities entering from the $\text{Li}(2S_{1/2})+\text{Ba}^+(5D_{5/2})$ or the $\text{Li}(2S_{1/2})+\text{Ba}^+(5D_{3/2})$ amounts to $P_T^{5/2} = 0.264$, $P_B^{5/2} = 0.982$ and $P_B^{3/2} = 0.979$. Including the statistical weights $1/12$ and $1/8$ for the initial population of the $\Omega = 0^+$ state within the $5D_{5/2}$ and $5D_{3/2}$ incoming channels yields $P_{\text{NRCE}}^{5/2} = P_T^{5/2}(1 - P_T^{5/2})(1 - P_B^{5/2})/6 = 0.0318$, $P_{\text{NRCE}}^{3/2} = (1 - P_B^{3/2})P_B^{3/2}/4 = 0.0051$, and $P_{\text{FSQ}}^{5/2} = P_T(1 - P_T)P_B^{5/2}/6 = 0.0006$.

Appendix F. Coupled-channel equations for quantum scattering

We first disregard the coupling between the mechanical rotation between the two particles ℓ and the internal angular momenta, so that the total wavefunction of the colliding pair can be expressed as a partial wave expansion, and each partial wave ℓ is treated independently. The corresponding Hamiltonian \mathbf{H}_ℓ considering the electronic interactions (PECs and SOCs) and the uncoupled rotation of the nuclei, can be described as

$$\mathbf{H}_\ell(R) = -\frac{\hbar^2}{2\mu} \frac{d^2}{dR^2} \mathbf{I} + \frac{\hbar^2 \ell(\ell+1)}{2\mu R^2} \mathbf{I} + \mathbf{V}(R) + \mathbf{V}_{\text{soc}}(R) \quad (\text{F1})$$

where μ is the LiBa^+ reduced mass, R is the internuclear distance, $\mathbf{V}(R)$ the electronic potential energy matrix, $\mathbf{V}_{\text{soc}}(R)$ the spin-orbit matrix, and \mathbf{I} the identity matrix. ℓ is the partial wave, i.e. the mechanical rotation of the colliding nuclei

in SF frame. We solve the coupled equations using log derivative method [56, 57] with a constant step-size 0.005 a.u. for a given collision energy E . Since the rotational interaction (varying as $1/R^2$) dominates the electrostatic interaction (varying as $1/R^4$), the scattering wavefunction is defined by Riccati-Bessel functions at infinity (actually 10 000 a.u. in the computations). We then extract the reaction matrix \mathbf{K} holding close and open channels and the scattering matrix \mathbf{S} containing only open channels.

We apply the same numerical approach for the MCQS calculations in the SF frame using the basis transformation defined in the appendix G

Appendix G. Frame transformation from Hund's case (a) in the BF frame to Hund's case (e) basis in the SF frame

To describe the states related to the $\text{Li}^+ + \text{Ba}$ and $\text{Li} + \text{Ba}^+$ dissociation limits, we use the properly symmetrized fully-coupled Hund's case (e) basis functions in the SF frame $|j_a j_b j \ell J M p\rangle$, where the quantum numbers are associated to the angular momenta $\vec{j} = \vec{j}_a + \vec{j}_b$, $\vec{J} = \vec{j} + \vec{\ell}$, M being the projection of \vec{J} on a quantization axis. The basis functions have a defined parity $p = (-1)^{L_a + L_b + \ell}$, where \vec{L}_{Li} and \vec{L}_{Ba} are the electronic angular momenta of the atoms. In the following, we omit M as we do not consider any external field.

In this basis the matrix elements H_{rot}^{ij} are simply equal to $\delta_{ij} \hbar^2 \ell_i (\ell_i + 1) / 2\mu R^2$, where ℓ_i denotes the rotational angular momentum in the channel i . The BF to SF frame transformation is applied to $V(R) + V_{\text{soc}}(R)$. The new $\overline{V(R)}$ is not diagonal and the $\overline{V_{\text{soc}}(R)}$ differs from the spin-orbit matrix in the FCLZ model.

In the BF frame, the projection of the total angular momentum J on the molecular axis is $\Omega = \Lambda + \Sigma$, where Λ and Σ are the projections of the electronic orbital \vec{L} and the spin angular momenta \vec{S} on the molecular axis, respectively. The molecular basis with parity $(-1)^p$ in Hund's case (a) is

$$\begin{aligned} |\Lambda\Sigma J p\rangle &= (2 - \delta_{\Lambda,0} \delta_{\Sigma,0})^{-1/2} \\ &\times \left\{ |\Lambda\Sigma J \Omega\rangle + (-1)^{J-S+p} \right. \\ &\times \left. (1 - \delta_{\Lambda,0} \delta_{\Sigma,0}) |-\Lambda S - \Sigma J - \Omega\rangle \right\} \end{aligned} \quad (\text{G1})$$

The transformation elements from (a) to (e) is obtained by

$$\begin{aligned} \langle j_a j_b j \ell J p | \Lambda\Sigma J M p \rangle &= (-1)^{\ell - \Omega - J} (2 - \delta_{\Lambda,0} \delta_{\Sigma,0})^{-1/2} \\ &\times \left[1 + (-1)^{L_a + L_b + \ell + p} (1 - \delta_{\Lambda,0} \delta_{\Sigma,0}) \right] \\ &\times \sqrt{(2S+1)(2j_a+1)(2j_b+1)} \\ &\times \langle l_0 | j - \Omega, J \Omega \rangle \langle L \Lambda | L_a \Lambda_a, L_b \Lambda_b \rangle \\ &\times \begin{Bmatrix} L_a & S_a & j_a \\ L_b & S_b & j_b \\ L & S & j \end{Bmatrix} \langle j \Omega | L \Lambda, S \Sigma \rangle \end{aligned} \quad (\text{G2})$$

where $\vec{L} = \vec{L}_a + \vec{L}_b$, $\Omega = 0^\pm, 1, 2, 3$, and the sharp and curly brackets denote $3j-$ and $9j-$ coefficients, respectively. When squared, these matrix elements determine the weights of

Table 4. The good quantum numbers for S+S, Ion+S and S+D dissociation limits for Hund's cases (a), (c) and (e), for even and odd J values, thus determining the correspondence with the total parity + and -. There is no line-to-line correspondence between the columns.

J - even/odd					
(a) (${}^S\Lambda_{ \Omega }$)		(c) ($ \Omega $)		(e) ($j_{\text{Li}}, j_{\text{Ba}}, j, l$)	
+/-	-/+	+/-	-/+	+/-	-/+
S+S					
${}^1\Sigma_0^+$	${}^3\Sigma_0^+$	0^+	0^-	$(\frac{1}{2}, \frac{1}{2}, 0, J)$	$(\frac{1}{2}, \frac{1}{2}, 1, J-1)$
${}^3\Sigma_1^+$	${}^3\Sigma_1^+$	1	1	$(\frac{1}{2}, \frac{1}{2}, 1, J)$	$(\frac{1}{2}, \frac{1}{2}, 1, J+1)$
Ion+S					
${}^1\Sigma_0^+$	—	0^+	—	$(0, 0, 0, J)$	$(0, 0, 0, J)$
S+D					
${}^1\Sigma_0^+$	${}^3\Sigma_0^+$	0^+	0^-	$(\frac{1}{2}, \frac{3}{2}, 1, J)$	$(\frac{1}{2}, \frac{3}{2}, 1, J-1)$
${}^3\Sigma_1^+$	${}^3\Sigma_1^+$	1	1	$(\frac{1}{2}, \frac{3}{2}, 2, J-2)$	$(\frac{1}{2}, \frac{3}{2}, 1, J+1)$
${}^1\Pi_1$	${}^1\Pi_1$	1	1	$(\frac{1}{2}, \frac{3}{2}, 2, J)$	$(\frac{1}{2}, \frac{3}{2}, 2, J-1)$
${}^3\Pi_0$	${}^3\Pi_0$	0^+	0^-	$(\frac{1}{2}, \frac{3}{2}, 2, J+2)$	$(\frac{1}{2}, \frac{3}{2}, 2, J+1)$
${}^3\Pi_1$	${}^3\Pi_1$	1	1	$(\frac{1}{2}, \frac{5}{2}, 2, J-2)$	$(\frac{1}{2}, \frac{5}{2}, 2, J-1)$
${}^3\Pi_2$	${}^3\Pi_2$	2	2	$(\frac{1}{2}, \frac{5}{2}, 2, J)$	$(\frac{1}{2}, \frac{5}{2}, 2, J+1)$
${}^1\Delta_2$	${}^1\Delta_2$	2	2	$(\frac{1}{2}, \frac{5}{2}, 2, J+2)$	$(\frac{1}{2}, \frac{5}{2}, 3, J-3)$
${}^3\Delta_1$	${}^3\Delta_1$	1	1	$(\frac{1}{2}, \frac{5}{2}, 3, J-2)$	$(\frac{1}{2}, \frac{5}{2}, 3, J-1)$
${}^3\Delta_2$	${}^3\Delta_2$	2	2	$(\frac{1}{2}, \frac{5}{2}, 3, J)$	$(\frac{1}{2}, \frac{5}{2}, 3, J+1)$
${}^3\Delta_3$	${}^3\Delta_3$	3	3	$(\frac{1}{2}, \frac{5}{2}, 3, J+2)$	$(\frac{1}{2}, \frac{5}{2}, 3, J+3)$

Hund's case (a) $|\Lambda\Sigma\Sigma\rangle$ channels in the Hund's case (e) channels. The relevant quantum numbers for S+S, Ion+S and S+D dissociation limits are summarized in table 4. We note that in the $|\Omega| = 0$ case, the parity of the ${}^1\Sigma_0^+$ (resp. ${}^3\Sigma_0^+$) state is + for even (resp. odd) J values. Thus for + parity, $|\Omega| = 0^+$ is involved only for even J , and $|\Omega| = 0^-$ for odd J . For - total parity the situation is reversed, i.e. $|\Omega| = 0^-$ only for even J values, and $|\Omega| = 0^+$ for odd J values.

Appendix H. Partial waves and shape resonances in the cross sections

For ${}^2D_{5/2}$ incoming channels and + parity (figures 12 and 13), we find a prominent shape resonance for both FSQ and NRCE processes around 10^{-4} K. In case of FSQ the resonance is mainly generated by $J = 4, 5$. Regarding the NRCE, only even J values contribute to the process, and $J = 2, 4$ are responsible for the appearance of the resonance. Due to the outstanding shape resonance the cross section for the FSQ process is slightly larger than the Langevin one. In case of - parity the FSQ process also dominates the NRCE process for which only odd J values contribute, and the cross section for the NRQ process is smaller with more than two orders of magnitude.

Regarding the ${}^2D_{3/2}$ incoming channels (figures 14 and 15), and for + parity up to 10^{-5} K the cross sections have similar behavior. In case of NRQ process the structure appearing around 10^{-4} K is created mainly by $J = 1, 3$, while around 10^{-3} K by $J = 5$. For the NRCE process the structure appearing at 4×10^{-5} K is the result of $J = 4$.

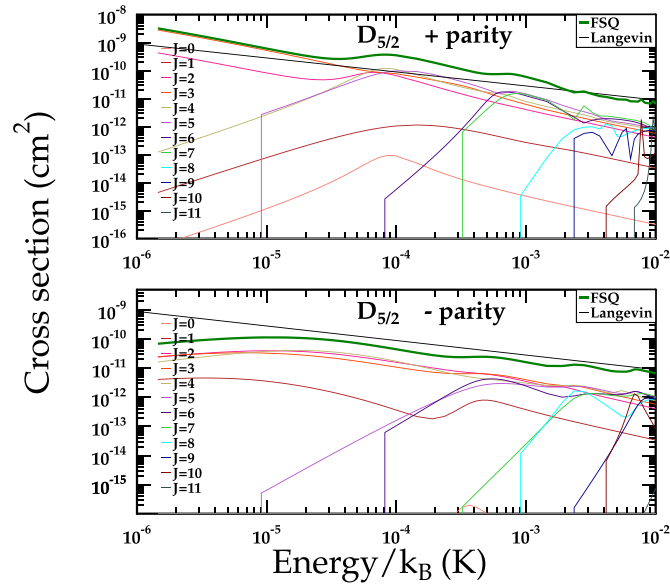


Figure 12. The parity dependent (thick green line) and the most relevant J -dependent partial cross sections (thin lines) for the FSQ process as a function of the temperature, for the $D_{5/2}$ incoming channels. For the + parity states at low temperatures $J = 3$ defines the character of the cross section, while at higher temperatures $J = 4$ then $J = 6$ becomes dominant. For the—parity states at low temperatures $J = 2$ and $J = 3$ defines the character of the cross section, while at higher temperatures $J = 6$ and $J = 8$ becomes dominant.

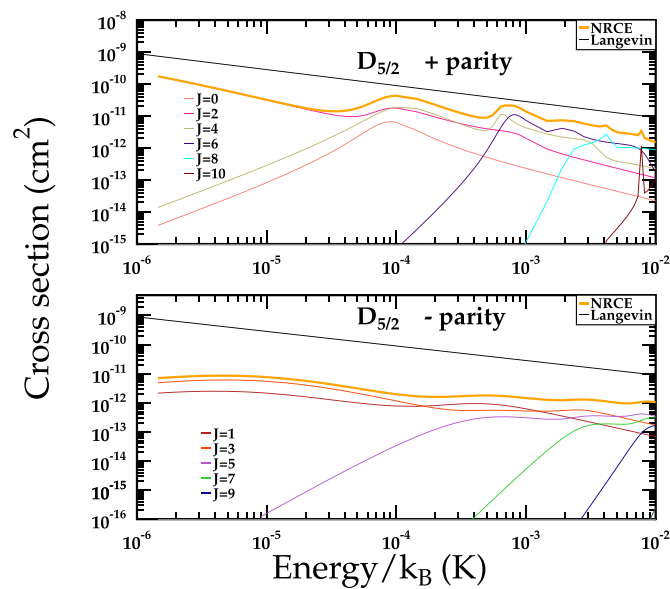


Figure 13. The parity dependent (thick yellow line) and the most relevant J -dependent partial cross sections (thin lines) for the NRCE process as a function of the temperature, for the $D_{5/2}$ incoming channels. For the + parity states at low temperatures $J = 2$ defines the character of the cross section, while at higher temperatures $J = 4$ then $J = 6$ becomes dominant. For the—parity states at low temperatures $J = 3$ and $J = 1$ defines the character of the cross section, while at higher temperatures $J = 5$ becomes dominant.

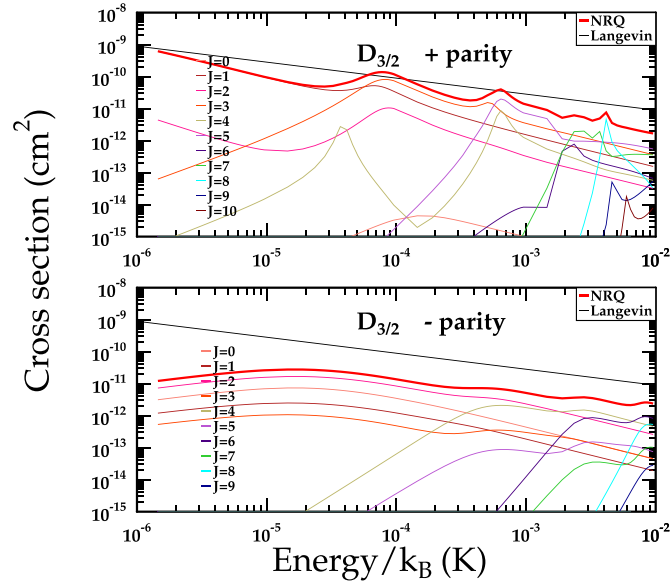


Figure 14. The parity dependent (thick red line) and the most relevant J -dependent partial cross sections (thin lines) for the NRQ process as a function of the temperature, for the $D_{3/2}$ incoming channels. For the + parity states at low temperatures $J = 1$ defines the character of the total cross section, while at higher temperatures $J = 3$ then $J = 5$ and $J = 8$ becomes dominant. For the - parity states at low temperatures $J = 2$ defines the character of the cross section, while at higher temperatures $J = 4$ and $J = 6$ becomes dominant.

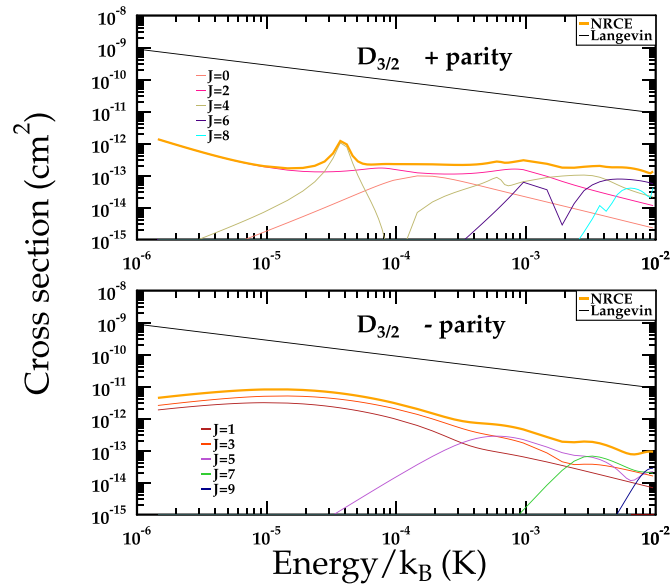













Figure 15. The parity dependent (thick yellow line) and the most relevant J -dependent partial cross sections (thin lines) for the NRCE process as a function of the temperature, for the $D_{3/2}$ incoming channels. For the + parity states almost through the whole temperature range $J = 2$ and $J = 4$ defines the character of the cross section. For the - parity states $J = 3$ then $J = 5$ and $J = 7$ becomes dominant. We note here that the NRCE process concerns only channels correlating to the $\text{Li}^+ + \text{Ba}(^1S)$ asymptote, which has exclusively $^1\Sigma^+$ character, thus for + parity case only even J , while for - parity case only odd J values contribute to the total cross section.

ORCID iDs

Xiaodong Xing  <https://orcid.org/0000-0001-6933-7048>
 Pascal Weckesser  <https://orcid.org/0000-0003-3457-5841>
 Fabian Thielemann  <https://orcid.org/0000-0003-4578-8500>
 Tibor Jónás  <https://orcid.org/0009-0000-7686-9560>
 Romain Vexiau  <https://orcid.org/0000-0003-1705-6716>
 Nadia Bouloufa-Maafa  <https://orcid.org/0000-0002-5493-3661>
 Kirk W Madison  <https://orcid.org/0000-0003-0331-3267>
 Andrea Orbán  <https://orcid.org/0000-0002-9692-6347>
 Ting Xie  <https://orcid.org/0000-0002-2601-2283>
 Tobias Schaez  <https://orcid.org/0000-0001-7014-1069>
 Olivier Dulieu  <https://orcid.org/0000-0001-9498-3754>

References

- [1] Baroni C Lamporesi G and Zaccanti M 2024 Quantum mixtures of ultracold atomic gases (arXiv:2405.14562)
- [2] Lous R S and Gerritsma R 2022 Chapter two - ultracold ion-atom experiments: cooling, chemistry and quantum effects *Adv. At. Mol. Phys.* **71** 65
- [3] Deiß M Willitsch S and Hecker Denschlag J 2024 Cold trapped molecular ions and hybrid platforms for ions and neutral particles *Nat. Phys.* **20** 713
- [4] Krüchow A Mohammadi A Härter A Hecker Denschlag J Pérez-Ríos J and Greene C H 2016 Energy scaling of cold atom-atom-ion three-body recombination *Phys. Rev. Lett.* **116** 193201
- [5] Dieterle T, Bergruber M, Hölzl C, Löw R, Jachymski K, Pfau T and Meinert F 2020 Inelastic collision dynamics of a single cold ion immersed in a Bose-Einstein condensate *Phys. Rev. A* **102** 041301
- [6] Mohammadi A, Krüchow A, Mahdian A, Deiß M, Pérez-Ríos J, da Silva H, Raoult M, Dulieu O and Hecker Denschlag J 2021 Life and death of a cold BaRb⁺ molecule inside an ultracold cloud of Rb atoms *Phys. Rev. Res.* **3** 013196
- [7] Pérez-Ríos J 2021 Cold chemistry: a few-body perspective on impurity physics of a single ion in an ultracold bath *Molec. Phys.* **119** e1881637
- [8] Chowdhury S and Perez-Ríos J 2024 Ion solvation in atomic baths: from snowballs to polarons *Nat. Sci.* **4** e20240006
- [9] Hirzler H, Trimby E, Gerritsma R, Safavi-Naini A and Pérez-Ríos J 2023 Trap-assisted complexes in cold atom-ion collisions *Phys. Rev. Lett.* **130** 143003
- [10] Pinkas M, Katz O, Wengrowicz J, Akerman N and Ozeri R 2023 Trap-assisted formation of atom-ion bound states *Nat. Phys.* **19** 1573–8
- [11] Grier A T, Cetina M, Oručić F and Vuletić V 2009 Observation of cold collisions between trapped ions and trapped atoms *Phys. Rev. Lett.* **102** 223201
- [12] Härter A, Krüchow A, Brunner A, Schnitzler W, Schmid S and Hecker Denschlag J 2012 Single ion as a three-body reaction center in an ultracold atomic gas *Phys. Rev. Lett.* **109** 123201
- [13] Sourav D and Rangwala. S A 2018 Cooling of trapped ions by resonant charge exchange *Phys. Rev. A* **97** 041401
- [14] Smith W W, Makarov O and Lin J 2005 Cold ion-neutral collisions in a hybrid trap *J. Mod. Opt.* **52** 2253
- [15] Schmid S, Härter A and Hecker Denschlag J 2010 Dynamics of a cold trapped ion in a Bose-Einstein condensate *Phys. Rev. Lett.* **105** 133202
- [16] Hall F H J, Aymar M, Bouloufa N, Dulieu O and Willitsch S 2011 Light-assisted ion-neutral reactive processes in the cold regime : radiative molecule formation vs. charge exchange *Phys. Rev. Lett.* **107** 243202
- [17] Ratschbacher L, Zipkes C, Sias C and Köhl M 2012 Controlling chemical reactions of a single particle *Nat. Phys.* **8** 649
- [18] Haze S, Hata S, Fujinaga M and Mukaiyama T 2013 Observation of elastic collisions between lithium atoms and calcium ions *Phys. Rev. A* **87** 052715
- [19] Hall F H J, Aymar M, Raoult M, Dulieu O and Willitsch S 2013 Light-assisted cold chemical reactions of barium ions with rubidium atoms *Molec. Phys.* **111** 1683
- [20] Joger J, Fürst H, Ewald N, Feldker T, Tomza M and Gerritsma R 2017 Observation of collisions between cold Li atoms and Yb⁺ ions *Phys. Rev. A* **96** 030703
- [21] Sikorsky T, Ben-shlomi Ziv Meir R, Akerman N, Ozeri R and Ozeri R 2018 Spin-controlled atom-ion chemistry *Nat. Commun.* **9** 920
- [22] Mills M, Puri P, Li M, Schowalter S J, Dunning A, Schneider C, Kotochigova S and Hudson E R 2019 Engineering excited-state interactions at ultracold temperatures *Phys. Rev. Lett.* **122** 233401
- [23] Li H, Jyothi S, Li M, Klos J, Petrov Brown A, Kotochigova S K R and Kotochigova S 2020 Photon-mediated charge exchange reactions between ³⁹K atoms and ⁴⁰Ca⁺ ions in a hybrid trap *Phys. Chem. Chem. Phys.* **22** 10870
- [24] Schmidt J, Weckesser P, Thielemann F, Schaez T and Karpa L 2020 Optical traps for sympathetic cooling of ions with ultracold neutral atoms *Phys. Rev. Lett.* **124** 053402
- [25] Hall F H J, Eberle P, Hegi G, Raoult M, Aymar M, Dulieu O and Willitsch S 2013 Ion-neutral chemistry at ultralow energies: dynamics of reactive collisions between laser-cooled Ca⁺ ions and Rb atoms in an ion-atom hybrid trap *Mol. Phys.* **111** 2020
- [26] Saito R, Haze S, Sasakawa M, Nakai R, Raoult M, Da Silva H, Dulieu O and Mukaiyama T 2017 Characterization of charge-exchange collisions between ultracold ⁶Li atoms and ⁴⁰Ca⁺ ions *Phys. Rev. A* **95** 032709
- [27] Ben-shlomi R, Vexiau R, Meir Z, Sikorsky T, Akerman N, Pinkas M, Dulieu O and Ozeri R 2020 Direct observation of ultracold atom-ion excitation exchange *Phys. Rev. A* **102** 031301
- [28] Xing X, da Silva Jr H Vexiau R, Bouloufa-Maafa N, Willitsch S and Dulieu O 2022 Ion-loss events in a hybrid trap of cold Rb-Ca⁺: photodissociation, blackbody radiation and nonradiative charge exchange *Phys. Rev. A* **106** 062609
- [29] Cetina M, Grier A T and Vuletić V 2012 Micromotion-induced limit to atom-ion sympathetic cooling in paul traps *Phys. Rev. Lett.* **109** 253201
- [30] Feldker T, Fürst H, Hirzler H, Ewald N V, Mazzanti M, Wiater D, Tomza M and Gerritsma R 2020 Buffer gas cooling of a trapped ion to the quantum regime *Nat. Phys.* **16** 413
- [31] Tomza M, Koch C P and Moszynski R 2015 Cold interactions between an Yb⁺ ion and a Li atom: prospects for sympathetic cooling, radiative association and feshbach resonances *Phys. Rev. A* **91** 042706
- [32] Weckesser P, Thielemann F, Wiater D, Wojciechowska A, Karpa L, Jachymski K, Tomza M, Walker T and Schaez T 2021 Observation of Feshbach resonances between a single ion and ultracold atoms *Nature* **600** 429
- [33] Thielemann F Siemund J von Schoenfeld D Wu W Weckesser P Jachymski K Walker T and Schaez T 2024

- Exploring atom-ion Feshbach resonances below the s-wave limit (arXiv:2406.13410)
- [34] Hirzler H, Lous R S, Trimby E, Pérez-Ríos J, Safavi-Naini A and Gerritsma R 2022 Observation of chemical reactions between a trapped ion and ultracold Feshbach dimers *Phys. Rev. Lett.* **128** 103401
- [35] Haze S, Saito R, Fujinaga M and Mukaiyama T 2015 Charge-exchange collisions between ultracold fermionic lithium atoms and calcium ions *Phys. Rev. A* **91** 032709
- [36] da Silva Jr H Raoult M, Aymar M and Dulieu O 2015 Formation of molecular ions by radiative association of cold trapped atoms and ions *New J. Phys.* **17** 045015
- [37] Weckesser P, Thielemann F, Hoenig D, Lambrecht A, Karpa L and Schaetz T 2021 Trapping, shaping and isolating of an ion Coulomb crystal via state-selective optical potentials *Phys. Rev. A* **103** 013112
- [38] Leschhorn G, Hasegawa T and Schaetz T 2012 Efficient photo-ionization for barium ion trapping using a dipole-allowed resonant two-photon transition *Appl. Phys. B* **108** 159
- [39] Aymar M and Dulieu O 2005 Calculation of accurate permanent dipole moments of the lowest $1^3\Sigma^+$ states of heteronuclear alkali dimers using extended basis sets *J. Chem. Phys.* **122** 204302
- [40] Aymar M, Guérout R and Dulieu O 2011 Structure of the alkali-metal-atom-strontium molecular ions : towards photoassociation and formation of cold molecular ions *J. Chem. Phys.* **135** 064305
- [41] Aymar M and Dulieu O 2012 The electronic structure of the alkaline-earth-atom (ca, sr, ba) hydride molecular ions *J. Phys. B* **45** 215103
- [42] Deiglmayr J, Aymar M, Wester R, Weidemüller M and Dulieu O 2008 Calculations of static dipole polarizabilities of alkali dimers: prospects for alignment of ultracold molecules *J. Chem. Phys.* **129** 064309
- [43] Sardar D and Naskar S 2023 Cold collisions between alkali metals and alkaline-earth metals in the heteronuclear atom-ion system $\text{Li} + \text{Ba}^+$ *Phys. Rev. A* **107** 043323
- [44] Akkari S, Zrafi W, Ladjimi H, Bejaoui M, Dhiflaoui J and Berriche H 2024 Electronic structure of ground and low-lying excited states of BaLi^+ molecular ion: spin-orbit effect, radiative lifetimes and Franck-Condon factor *Phys. Scripta* **99** 035403
- [45] Cimiraglia R, Malrieu J P, Persico M and Spiegelmann F 1985 Quasi-diabatic states and dynamical couplings from ab initio CI calculations: a new proposal *J. Phys. B: Atom. Mol. Phys.* **18** 3073
- [46] Angeli C and Persico M 1996 Quasi-diabatic and adiabatic states and potential energy curves for Na-Cd collisions and excimer formation *Chem. Phys.* **204** 57
- [47] Landau L and Lifchitz E 1967 *Mécanique Quantique-Théorie Non-Relativiste* (Mir)
- [48] Orbán A, Vexiau R, Kriegelsteiner O, Nägerl H-C, Dulieu O, Crubellier A and Bouloufa-Maafa N 2015 Model for the hyperfine structure of electronically excited KCs molecules *Phys. Rev. A* **92** 032510
- [49] Gao B 2013 Quantum-defect theory for $-1/r^4$ -type interactions *Phys. Rev. A* **88** 022701
- [50] Langevin P 1905 *Ann. Chim. Phys.* **5** 245 (available at: <https://gallica.bnf.fr/ark:/12148/bpt6k34935p/f260.item>)
- [51] Tscherbul T V, Brumer P and Buchachenko A A 2016 Spin-orbit interactions and quantum spin dynamics in cold ion-atom collisions *Phys. Rev. Lett.* **117** 143201
- [52] Cairncross W B, Gresh D N, Grau M, Cossel K C, Roussy T S, Ni Y, Zhou Y, Ye J and Cornell E A 2017 Precision Measurement of the Electron's Electric Dipole Moment Using Trapped Molecular Ions *Phys. Rev. Lett.* **119** 153001
- [53] Dion C M, Drag C, Dulieu O, Laburthe Tolra B, Masnou-Seeuws F and Pillet P 2001 Resonant coupling in the formation of ultracold ground state molecules via photoassociation *Phys. Rev. Lett.* **86** 2253
- [54] Berkeland D J, Miller J D, Bergquist J C, Itano W M and Wineland D J 1998 Minimization of ion micromotion in a Paul trap *J. Appl. Phys.* **83** 5025–33
- [55] Śmiałkowski M and Tomza M 2020 Interactions and chemical reactions in ionic alkali-metal and alkaline-earth-metal diatomic ab^+ and triatomic a_2b^+ systems *Phys. Rev. A* **101** 012501
- [56] Johnson B R 1973 The multichannel log-derivative method for scattering calculations *J. Comput. Phys.* **13** 445
- [57] Alexander M H and Manolopoulos D E 1987 A stable linear reference potential algorithm for solution of the quantum close-coupled equations in molecular scattering theory *J. Chem. Phys.* **86** 2044